MICROFLUIDIC HYDRODYNAMIC FOCUSING FOR FLOW CYTOMETRY AND DIFFUSION-MIXING

A Dissertation

Presented to the Faculty of the Graduate School

of Cornell University

In Partial Fulfillment of the Requirements for the Degree of

Doctor of Philosophy

by

Matthew John Kennedy

May 2010

MICROFLUIDIC HYDRODYNAMIC FOCUSING FOR FLOW CYTOMETRY AND DIFFUSION-MIXING

Matthew John Kennedy Ph. D.

Cornell University 2010

Microfluidics provides a unique and useful platform for performing analytical measurements. Micro-optics can be imbedded into a microfluidic device, and the analyte can be maneuvered hydrodynamically into the optical interrogation zone. In addition, since flow is laminar, the concentration distributions of the solutes can be explicitly calculated over the volume of the device.

In this work, a microfluidic hydrodynamic focusing manifold was developed which focused a solution into the center of a square microfluidic channel. By adjusting the flow-rates of the focusing fluids, the solution-under-focusing was moved up and down relative to the top and bottom walls of the microchannel.

In one embodiment, the hydrodynamic focusing manifold was integrated with imbedded optical fibers for use as a micro- flow cytometer. By hydrodynamically aligning the particle stream with the laser beam, absolute counting efficiency of 58±8% was demonstrated for fluorescent microparticles at a throughput of 5.5 μL/min of bead solution. This device can be used to analyze a multiplexed bead-based assay for point-of-detection biosensing.

In a second embodiment, the focusing manifold fed into a long microchannel where solute-mixing took place under pressure-driven laminar flow conditions. A numerical analysis program was developed which modeled the three-dimensional microfluidic channel with a two-dimensional mesh by using the moving mesh method. Using this

program, concentration distributions were calculated at distances along the microchannel, and these were compared to an imaging experiment. The numerical analysis program overestimated the diffusion coefficients of fluorescein and Enhanced Green Fluorescent Protein by factors of 1.9 ± 0.4 and 1.4 ± 0.2, respectively. The source of this overestimation was hydrodynamic dispersion, the effect of which could not be properly treated using the moving mesh method due to the assumption transverse-uniform fluid-velocity over the cross-section of the microchannel. Advances in numerical analysis are needed for improved modeling and characterization of microfluidic devices, particularly those for which the two effects of hydrodynamic dispersion and molecular diffusion simultaneously influence the movements of the solutes.

This dissertation informs the development of microfluidic analytical devices and the analysis of solute-transport within microfluidic channels.

BIOGRAPHICAL SKETCH

Matthew John Kennedy was born the son of Hal Avon Kennedy and Deborah Mary Kerekes in Upland, California, USA on May 14, 1982. Matt developed an early fascination with the family personal computer, and he became a self-taught computer programmer in QBASIC at age 13. Matt obtained his B.S. in physics with a strong emphasis in mathematics from the University of California in Los Angeles in May of 2004. As an undergraduate, Matt worked as a research assistant, first for an applied mathematician, Paul H. Roberts, and then for a seismologist, John E. Vidale. These experiences provided Matt with backgrounds in numerical analysis and digital signal processing, respectively. Hoping to learn hands-on experimental skills, Matt entered graduate school in engineering at Cornell University in the fall of 2004. At Cornell, he found a group specializing in interdisciplinary hands-on science, under the direction of Professor Carl A. Batt, and within this group he began developing and characterizing lab-on-a-chip devices. When not in the lab, Matt could often be found at the bowling alley or working the evening shift at the Big Red Barn.

ACKNOWLEDGMENTS

Thank you Carl Batt for all of the support and for always keeping things interesting. Thank you fellow labmembers for contributing your wide range of knowledge and for all of the extracurricular activities. In particular, thank you Scott Stelick and Nathan Cady for getting me started when I first showed up in the lab. An additional thank you to Scott Stelick for imparting on me during my first years a useful set of skills in microengineering and instrumentation.

Shared facilities made my research possible. Significant portions of this work were performed at the Cornell Nanofabrication Facility (CNF), the Cornell Microscopy and Imaging Facility (MIF), the Cornell Machine Shop, and the Cornell Core Flow Cytometry Facility. Thank you to the technical staff and users at all three of these facilities. In particular, thank you Carol Bayles at the MIF for helping me develop the confocal microscopy imaging protocol, and thank you Nathan at the machine shop for helping me construct the shielding encasements for the photodetectors.

My research experience was greatly enhanced by undergraduate and M.Eng. students whom I had the privilege to mentor. In particular, thank you Sasha L. Perkins for your productive summer improving the design and exploring potential applications of the microfluidic hydrodynamic focusing device. Also, thank you Li Cao for developing the ANSYS simulation program.

Thank you to my undergraduate research advisors, John Vidale, Paul Roberts, and Charles Whitten, for infusing me with an enthusiasm for research.

Thank you to my graduate student peers for the all of the fun times and for helping me to maintain my sanity.

Finally, thank you to my parents and sister for demanding that I complete this dissertation and move on with my life.

TABLE OF CONTENTS

LIST OF FIGURES

LIST OF TABLES

PREFACE

Microfluidic devices have not yet been commercially developed to the point of mainstream use. Unlike the microelectronics community, which benefited from the development of the personal computer, the microfluidics community has not yet found a 'killer app' (Whitesides 2006). Still, considerable advances have been made towards the adoption of microfluidic devices particularly with regard to materials and fabrication. Twelve years ago a method was reported for rapidly prototyping microcfluidic devices (Duffy, McDonald et al. 1998). Using this rapid prototyping technique, a large number of devices can now be replica-molded in a short time. The material used for rapid prototyping is poly(dimethylsiloxane), a flexible elastomer. This material is optically transparent making it simple to perform optical analysis on prototype microfluidic devices. In addition, the flexibility and robustness of the material has led to the development of integrated valves and pumps, allowing for complex sequences of steps to be implemented entirely on-chip.

When I first entered the Ph.D. program, a number of researchers were shrinking conventional analytical biosensor instruments onto microfluidic devices in order to develop portable biosensors. For example, just prior to my arrival in Carl Batt's laboratory, labmembers demonstrated a portable microfluidics-based instrument for detecting *Listeria monocytogenes* using PCR (Cady, Stelick et al. 2005). Under guidance from Cady, Stelick and Batt, I began developing a micro- flow cytometer with the goal of simultaneously detecting multiple targets using spectrally encoded beads. This concept had already been demonstrated using commercial instruments, and the challenge was simply to implement the technique on a chip. While conceptually simple, the execution of this project was more difficult than I had anticipated due to some wheels that required reinventing particularly with regard to

data acquisition and data processing.

During my years as a Ph.D. student, flow cytometry was explored not only by myself but by numerous other groups around the world due to its perceived potential as the 'killer app'. The flow cytometer is one of the simplest conceivable microsystems one can develop; particles are simply directed through an illuminating beam. In addition, many flow cytometry measurements would be better-performed at the point-of-detection, such as environmental monitoring of plankton populations or the counting of T-cells in rural parts of the world in the fight against AIDS.

As of today, a growing number of microfluidics researchers have focused their efforts on the development of novel analytical techniques that were not possible using conventional instrumentation. For example, using laminar flow it is possible to focus a solution into a subregion of the microfluidic channel and then allow for diffusion to occur between the focusing fluids and the solution-under-focusing. Unlike conventional turbulent flow, where mixing is unpredictable and the flow-paths are unique each time an experiment is repeated, within microfluidic channels the mixing is predictable and same flow-paths are repeated from experiment to experiment. For this reason, hydrodynamic focusing devices have been used to study protein-folding, since the predictable nature of laminar flow allows the concentration distributions of the solutes to be calculated at the locations of observation.

In the first chapter of this work, a microfluidic hydrodynamic focusing device is presented that is capable of focusing a solution into the center of a microfluidic channel and which can, furthermore, maneuver the solution-under-focusing up and down via the flow-rates of the focusing fluids.

In the second chapter, the microfluidic hydrodynamic focusing device is integrated with imbedded optical fibers for use as a flow cyometer. It is shown that the optical alignment can be optimized hydrodynamically by maneuvering the analyte-stream up

and down relative to the fixed illuminating beam.

In the third chapter, the focusing device is fed into a long microfluidic channel where diffusive mixing takes place. Whereas previous diffusion mixers were suited for the analysis of proteins, due to its larger orifice the present device is suited for the analysis of cells. A numerical model is developed for analyzing the species-transport under laminar-flow conditions, and the model is compared with experiment.

REFERENCE

Cady, N. C., S. Stelick, et al. (2005). "Real-time PCR detection of Listeria monocytogenes using an integrated microfluidics platform." Sensors and Actuators B **107**: 332-341.

Duffy, D. C., J. C. McDonald, et al. (1998). "Rapid Prototyping of Microfluidic Systems in Poly(dimethylsiloxane)." Analytical Chemistry **70**(23): 4974-4984.

Whitesides, G. M. (2006). "The origins and future of microfluidics." Nature **442**: 368-373.

CHAPTER 1

HYDRODYNAMIC FOCUSING WITH A MICROLITHOGRAPHIC MANIFOLD: CONTROLLING THE VERTICAL POSITION OF A FOCUSED SAMPLE

Adapted from: Kennedy, M. J., Stelick, S. J., Perkins, S. L., Cao, L., Batt, C. A. Hydrodynamic focusing with a microlithographic manifold: Controlling the vertical position of a focused sample. *Microfluidics and Nanofluidics* (2009). Reproduced with permission from Springer.

ABSTRACT

A microfluidic manifold has been designed, fabricated, and tested that hydrodynamically focuses a sample into the center of a microchannel and provides control over the vertical position of the sample via the flow-rates of the focusing fluids. To characterize the focusing action, a mixing experiment was performed in which the sample fluid and focusing fluid contained two spectrally independent fluorescent dyes. By sweeping the ratio of the rate of the top focusing fluid to the rate of the bottom focusing fluid, the sample was positioned first near the top of the microchannel and then translated downward in steps to the bottom of the microchannel. Images were optained with confocal microscopy, and the presumptive concentration distributions were computed using multiphysics software. The simulations were shown by direct visual comparison with the experimental images to accurately predict the distributions of fluids in our device. In order to quantitatively compare the two data sets, the images and simulations were analyzed using a simple center-of-mass measurement, and according to this measurement, the simulations accurately predicted the vertical position of the focused sample.

1. Introduction

Microfluidic manifolds are becoming important for applications in flow cytometry (McClain, Culbertson et al. 2001), gellation of microfibers (Shin, Park et al. 2007), self-assembly of nanoparticles (Laulicht, Cheifetz et al. 2008), and the study of protein folding (Pollack, Tate et al. 2001). Focusing in microscale laminar flow devices has been achieved via several mechanisms including dielectrophoresis (Holmes, Morgan et al. 2006), electro-osmosis (Kohlheyer, Unnikrishnan et al. 2008), optical gradient

(Zhao, Fujimoto et al. 2007), ultrasound (Goddard, Sanders et al. 2007), and hydrodynamic pressure. Hydrodynamic focusing is the method employed in this study and is achieved by applying a pressure differential across the inputs and output(s) of the manifold.

Vertical steering of a centrally focused fluid stream in a planar microfluidic device is useful for developing portable optical biosensors. Optical biosensors historically have relied on mechanical micropositioning equipment to align the flow-cell with the optical detection system. In the development of microfabricated flow cytometers, several groups have taken steps to eliminate the micropositioning equipment by imbedding integrated optics directly into the flow-cell (Fu, Yang et al. 2004; Tung, Zhang et al. 2004; Wang, El-Ali et al. 2004). In such static arrangements where the optical components remain permanently fixed in their positions, the ability to control the vertical position of the particle stream by adjusting the flow-rates of the focusing fluids provides an attractive method for tuning the alignment between the sample and the optical detection system.

The first microfluidic hydrodynamic focusing devices focused a sample from two sides into a thin columnar stream (Knight, Vishwanath et al. 1998). Initial designs for focusing not only from the sides but also from above and below involved several fabrication steps with as many as five-layers of manifold housing (Sundararajan, Pio et al. 2004). Recent efforts have focused on fabrication simplicity. Manifolds capable of out-of-plane focusing have been constructed from two planar microfluidic layers (Nieuwenhuis, Bastemeijer et al. 2003; Simonnet and Groisman 2005; Chang, Huang et al. 2007); these devices function by overlapping the channels of the first layer with those of the second layer at junctions where the sample is impinged by fluid from the adjoining layer. Using several stages of focusing, Nieuwenhuiset al. focused a sample from above, below, and from the sides, thereby maneuvering the sample into the

geometric center of the microchannel. By adjusting the flow-rates of the various fluid inputs, the focused stream was moved up and down and also to the sides, as demonstrated by finite element simulations and brightfield microscopy. Similar devices consisting of four focusing stages (Simonnet and Groisman 2005) and three focusing stages (Chang, Huang et al. 2007) were subsequently studied using single-color confocal microscopy. In these studies, cross-sectional confocal microscopy images were obtained showing the sample focused into a stream small in cross-section compared with the dimensions of the microchannel.

Here, we describe a two-layer manifold following the same design concept as (Chang, Huang et al. 2007) but containing only two-stages of focusing instead of three-stages. This advance reduces the number of fluid inputs required to achieve three-dimensional focusing.

The effect of adjusting the upper and lower focusing flow-rates on the distribution of fluids in our device was investigated by performing a mixing experiment in which the sample fluids contained fluorescein and the focusing fluids contained rhodamine. Images were obtained under a confocal microscope, and concentration distributions were extracted from these images using a series of image processing procedures. For comparison with the experimental images, the presumptive concentration distributions were computed using ANSYS computational fluid dynamics software. To the knowledge of the authors, this is the first study in which a microfluidic focusing manifold has been imaged by two-color confocal microscopy, and this is the first study in which the center-of-mass of the focused stream has been measured relative to the top and bottom walls of the microchannel by analysis of cross-sectional confocal microscopy images. In this paper, we present direct and quantitative comparisons between the images and the simulations, and we demonstrate the capability of this new manifold for controlled out-of-plane steering of the focused sample.

2. Description of the manifold

The manifold was constructed from two complementary pieces of polydimthyl siloxane (PDMS). The dimensions of the manifold were h = 125 μm, w_1 = 125 μm, w_2 = 50 μm, and w_3 = 50 μm, as illustrated in Figure. 1a. The sample was applied to the first input at volumetric rate U_1, and focusing fluid was applied to the second and third inputs at volumetric rates U_2 and U_3, as illustrated in Figure 1b. The flow-cell contained a total of five fluid inputs. Focusing fluid was applied at each focusing stage by a symmetric pair of fluid inputs from opposite sides of the main microchannel; therefore, the total flow-rate was $U_{TOT} = U_1 + 2U_2 + 2U_3$. For the duration of the experiment, the flow-cell was operated under continuous flow conditions at Reynolds number Re = 2.72, which corresponds to a total volumetric flow-rate of $U_{TOT} = 20.4\,\mu$L/min (2.20 cm/s), for all measurements. Also, the ratio of sample fluid to total fluid was fixed at $U_1 / U_{TOT} = 1/10$.

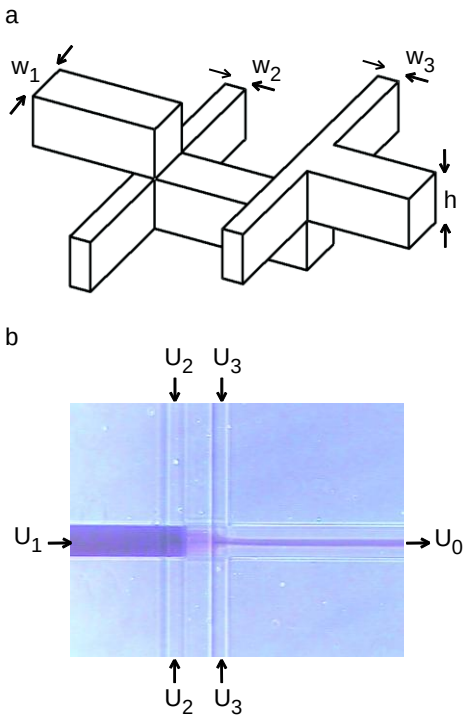

Figure 1. Schematic and optical micrograph of the hydrodynamic focusing manifold. a Schematic shows the geometry and dimensions. The height of all features was h. The width of the microchannel guiding the fluid under focusing was w_1. The widths of the microchannels guiding the focusing fluids were w_2 and w_3. b Optical micrograph shows the device with food coloring added to the fluid-under-focusing. The fluid under focusing was applied at volumetric rate U_1 (μL/min), and the focusing fluids were applied at rates U_2 and U_3 at the first and second focusing junctions.

3. Methods

3.1. Fabrication

The flow-cell was fabricated by bonding together two patterned pieces of PDMS using a contact-aligner. Briefly, two polydimethylsiloxane (PDMS) masters were fabricated by patterning polyimide resist onto silicon wafers with photolithography. A thickness of resist of 125 μm was obtained by applying two rounds of spin-coating of SU8-75 (Microchem Corporation, USA) at 2375-RPMs for 40 s for each silicon wafer. Each round of spin-coating was followed by 20-min baking at 95ºC on a hotplate. After cooling, the coated wafer was exposed to ultraviolet light through a patterned chrome mask and then post-exposure baked for 12 min at 95ºC. The wafers were chemically developed to remove resist from all unexposed locations and then rinsed with water followed by Isopropyl Alcohol. After rinsing, PDMS was spun onto the masters at 250 RPMs for 60 s in order to obtain molds of uniform thickness for the subsequent contact alignment procedure. The PDMS was then cured by baking at 70°C for 45 min.

The critical step in the fabrication of this flow-cell was the alignment of the two pieces of PDMS relative to one another as they were brought into contact. Immediately preceding alignment, the two pieces were peeled from their masters and exposed to a 200-W oxygen plasma (Glen Technologies 1000p), patterned side up, for 20-seconds. Next, the pieces were placed into aligned contact using a contact aligner (III-HR, Hybrid Technology Group, USA) and subsequently baked for 30 min at 70°C to achieve permanent bonding. The flow-cells were packaged by connecting tubing lines (Tygon Tubing PVC .020", Small Parts, Inc.) to the input of each fluid channel via 27-gauge stainless steel tubing (Small Parts, Inc.).

3.2 Simulations

Analysis of two-species transport was performed using commercially available finite element-based software. The flow-cell geometry was defined in ANSYS Multiphysics 10.0 as a 3D FLOTRAN-142 element and meshed with an element edge length of 5-μm. A load of Species 1, molecular weight 480 g/mol in water, corresponding to fluorescein, was applied to the central input, and a load of Species 2, molecular weight 330 g/mol in water, corresponding to rhodamine, was applied to the focusing inputs. A mass diffusion coefficient of $5e^{-6}\mu m^2/s$ was assumed for both species. A steady-state solution was obtained by solving, together, the Navier-stokes equation and the convection-diffusion equation using 60-global iterations of the ANSYS preconjugated residual method solver. From this solution, a contour plot was obtained of the concentration distribution of fluorescein over the volume of the manifold. The color-map was defined in ANSYS such that the range of normalized values of concentration, [0, 1], mapped linearly to the range of pixel values [0, 255]. One contour plot was obtained for the concentration of fluorescein and another contour plot was obtained for the concentration of rhodamine. The two contour plots were exported as TIF files and then, using ImageJ Image Processing Software, were overlayed onto the same image. Cross-sectional images were obtained by altering the viewpoint in ANSYS from 3-D view to cross-sectional view and then repeating the export and overlay procedure.

3.3 Confocal Microscopy

Experimental images of the distributions of fluids were obtained using an inverted laser-scanning spectral confocal microscope (LSM 510-META, Zeiss, Inc.). The microscope is fitted with two excitation sources: a 30-mW Argon Laser (471 nm, 488 nm) and a 15-mW diode-pumped solid-state laser (561 nm). The microscope acquires

spectral image data by using a grating to disperse the signal onto a multidetector array. One detector was filtered to detect fluorescence from the fluorescein-labeled fluids in the range of 505-555 nm, and the other detector was filtered to detect fluorescence from the rhodamine-labeled fluids in the range of 575-650 nm. Line-wise multi-tracking was used to further reduce spectral cross-talk by eliminating the simultaneous emission of both chromophores by both excitation sources. Multi-tracking refers to the electronic control of the scanners and laser lines to switch the excitation wavelength between line-scans (Dickinson, Bearman et al. 2001). Moreover, the 471-nm line of the Argon laser was used for excitation of the fluorescein because the shorter-wavelength mode of excitation reduced the spectral bleedthrough of fluorescence from rhodamine into the green-channel PMT compared to the 488-nm line.

The flow-cell was mounted on the sample holder of the microscope and syringe pumps were placed in proximity (PHD 2000, Harvard Instruments). The sample contained 0.2 mM fluorescein in Tris Buffer pH 8.0, and the sheath fluid contained 0.2 mM Rhodamine 6G in water. Particulates were eliminated from both solutions prior to the experiment using 0.45-μm syringe filters (21053-25, Corning, USA). The flow-cell was operated under continuous-flow conditions at Reynold's number Re=2.7 for the duration of the experiment. Between adjustment to the flow-rates and the acquisition of an experimental image, 5 min time was allowed to pass to ensure that each image represented the steady-state distribution. On a few occasions, instabilities arose when an air bubble entered the microchannel as verified by direct observation through the eyepieces of the microscope. When this occurred, time was allowed until the air bubble had passed, and then an image was recorded after the fluids had returned to their steady-state distribution.

Images were scanned through a cross-section of the channel using a 20X microscope

objective. The distance between the depth of successive scan-lines was 1.0 μm, and the total depth of the yz-scan was typically 160 μm. The horizontal scan-resolution was 0.29 μm, and the width of the scan was 148 μm. Therefore, a raw yz-scan typically contained 512 x 160 rectangular pixels. These data were extrapolated by the Zeiss LSM Imaging Software accompanying the microscope to deliver images containing square-pixels, with each pixel representing an area of 0.29 μm x 0.29 μm. The resulting two-color images typically contained 512 x 554 pixels, and these were exported as TIF files for subsequent processing and analysis.

3.4. Image Analysis

Images were imported into MATLAB for processing. Each pixel contained values for red, green, and blue, and the blue pixel-values were all zero. Therefore, each image could be thought of as an overlay of one green image and one red image onto the same grid of pixels, where the red image contained intensity values detected by the red-channel PMT, $I_R(x, y)$, and the green image contained the intensity values detected by the green-channel PMT $I_G(x, y)$. Therefore, each pixel contained red-values I_R and green-values I_G each in the range of 0–255.

(i) Image registration

Our image registration fit the walls of the microchannel with a rectangle by first segmenting the image and then fitting the segmented image with horizontal and vertical lines. Segmentation was achieved with the Sobel Operator using the *edge()* function in MATLAB. Next, a horizontal line was fit to the top edge by minimizing the sum of the squares of differences between the pixels of the detected top edge and the horizontal line. The bottom edge and the left and right edges were then obtained in the same manner. The error associated with locating the top and bottom walls of the

microchannel was estimated by calculating the standard deviation of the Sobel-detected pixels about the fitted edge; specifically, $\sigma = \sqrt{\frac{1}{N}\sum_{i=1}^{N}(y_i - y_{FIT})^2}$. This error did not change noticeably during the sweeping of the focusing flow-rates.

(2) Spectral unmixing

Spectral unmixing was performed in order to remove the contribution of rhodamine fluorescence from the pixel green-values of the images. Briefly, a specific fraction of the red-pixel-values were subtracted from the green pixel-values of the images. This fraction was calculated from the flat-field image in which all of the fluids were loaded with rhodamine, as explained in detail in Appendix 1.

(ii) Depth-dependence compensation

Depth-dependence compensation was performed according to a linear mathematical correction method. Briefly, the brightness of the image was observed to decay with depth. The slope of decay of brightness was measured separately for the red-pixel-values and the green-pixel-values by analyzing field images in which the microchannel contained only rhodamine or only fluorescein, respectively. Based on these calculations, the depth-decay was removed from the experimental images using a linear transformation, as explained in detail in Appendix 1.

3.5. Locating the center of mass of the fluorescein

The image analysis program calculates the center of mass of the fluorescein-labeled fluid according to the usual formula:

$$y_{CM} = \frac{\sum_{i,j} y_j \cdot I'_G(x_i, y_j)}{\sum_{i,j} I'_G(x_i, y_j)},$$

where x_i and y_i refer to pixels measured relative to the best-fit horizontal and vertical walls of the microchannel and I'_G refers to the green pixel-values of the image post-processing. This calculation was implemented in MATLAB using a *for* loop. The error associated with measuring the value of the center of mass, y_{CM}, was dominated by the error associated with measuring the location of the bottom and top walls of the microchannel, which was described in Sect. 3.4.

4. Results and discussion

4.1 Simulation

The concentration distributions of fluorescein and rhodamine were calculated over the volume of the manifold using ANSYS Multiphysics Computational Fluid Dynamics Software. Our simulations predicted that the sample would become sheathed on all sides in a cylindrical manner as shown in Figure 2a, where the ratio of the rate of the top focusing fluid to the rate of the bottom focusing fluid was $U_3 / U_2 = 1.5$. The focusing takes place in two steps: at the first junction, the sample is impinged from below by focusing fluids from the bottom layer, and at the second junction, the sample is impinged from above by focusing fluids from the top layer, as shown in Figure 2b. A vertical slice through the center of the channel along the direction of flow is shown in Figure 2c.

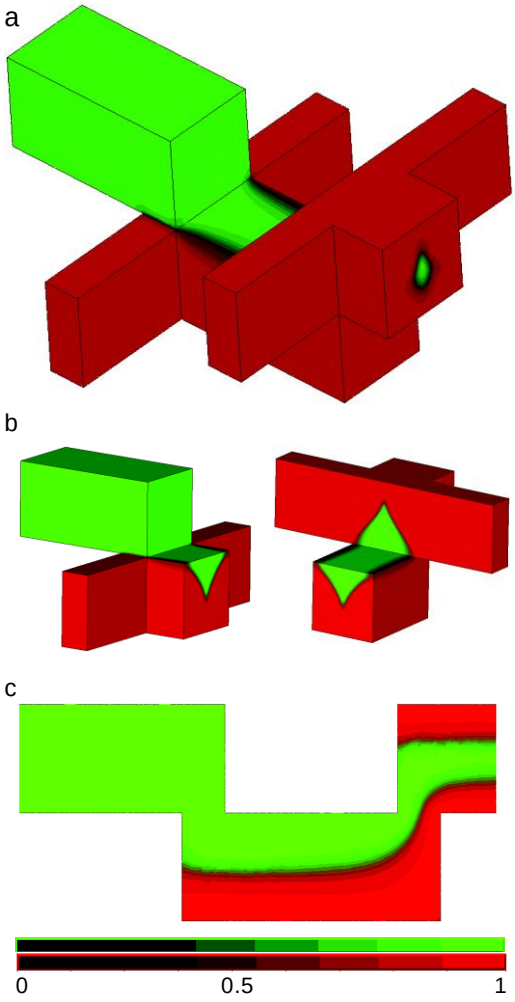

Figure 2. ANSYS simulations of two-species mixing. Concentration distributions are shown where the sample fluid contained fluorescein and the focusing fluid contained rhodamine. a Three-dimensional view; b three dimensional view broken into two pieces showing the species distributions between the first and second stages of focusing. c Cross-sectional view taken vertically through the center of the main channel along the direction of flow. The flow conditions used for the simulations shown in this image were Reynolds number Re = 2.7, focusing ratio U_3/U_2 = 1.5, and sample-to-total fluid fraction U_1/U_{TOT} = 1/10. These parameters corresponded to individual flow-rates of U_1 = 2.04 µL/min, U_2 = 3.67 µL/min, and U_3 = 5.51 µL/min.

4.2 Microscopy

The distribution of fluids at the output of the manifold was imaged by scanning through the depth of the channel using a confocal microscope. The focusing ratio, U_3/U_2, was varied, and several images were obtained. For small values of U_3/U_2, the sample was positioned near the top of the microchannel as shown in Figure 3a, whereas for large values of U_3/U_2, the sample was positioned near the bottom of the microchannel as shown in Figure 3e. In the case of $U_3/U_2 = 1.5$, the sample fluid was sheathed on all sides and was positioned near the geometric center of the microchannel as shown in Figure 3c.

Similar distributions were observed in the simulations and the experimental images regarding not only the vertical position of the focused stream but also the shape of the focused stream. For example, when the top and bottom focusing fluids were applied at similar rates, the focused stream took the form of an ellipse with a height of approximately twice its width, as seen by inspection in Figure 3c. In contrast, when the top focusing fluids were applied at a rate greater than the bottom focusing fluids, the fluorescein stream took the form of an isosceles triangle with its base lying along the bottom wall of the microchannel, as in Figure 3e. Notably, the shapes of the distribution of fluids were incongruent for the cases wehre the sample was positioned near the top versus the bottom of the microchannel (compare Figure 3a,e). We suggest that this incongruence arose from an absence of reflection symmetry in the geometry of the manifold about the plane dividing the main microchannel into its upper and lower halves, i.e., the plane at y=0.5.

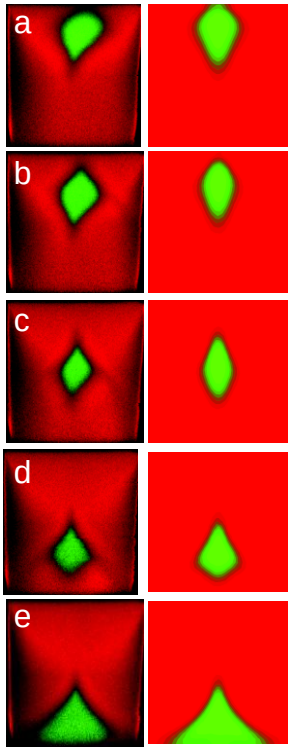

Figure 3. Fluorescence micrographs and simulations showing the distribution of the fluids at the output of the manifold. Confocal microscopy images are shown at left and simulations are shown at right for U_3/U_2 equal to a .012, b .20, c 1.5, d 11, and e 190

4.3 Image Analysis

Images were processed and then measured to yield the vertical position of the center of mass of the fluorescein-containing fluids. For this purpose, an image analysis program was written in MATLAB so that all images were processed and analyzed using the same sequence of steps. Our program consisted of four procedures: (1) image registration, (2) spectral unmixing, (3) depth-dependence compensation, and (4) measurement of the center of mass of the fluorescein-labeled fluids. The first procedure aligned the images to a common origin; the second and third procedures restored the images of two optical effects: spectral bleed-through and depth-dependence of fluorescence intensity; the fourth procedure provided a quantitative measurement describing the location of the focused sample.

(i) Image Registration

An image registration procedure was developed to locate the geometric center of the microchannel in each image. This provided a reference point to which the various images were subsequently aligned. Alignment of the images was necessary because the microscope drifted slightly during the time between the acquisition of successive images. The procedure first detected the walls of the microchannel using the Sobel Edge Operator, as shown in Figure 4b. Next, the channel dimensions were approximated as a rectangle by fitting the Sobel-detected edges with the best-fit horizontal and vertical lines, as shown in Figure 4c. The height of the channel was measured to be $h = 130 \pm 2$ μm and the width of the channel was measured to be $w = 128 \pm 2$ μm. The uncertainty in measuring w arose from the fabrication process- the microchannel was not completely square; specifically, the microchannel was slightly wider at the top than the bottom. The uncertainty in the measurement of h was a consequence, in part, of the distance in depth between successive scan-lines or 1 μm. The error associated with measuring the location of each wall of the

microchannel was estimated by calculating the standard deviation of the Sobel-detected edge pixels about the best-fit line to the wall of the microchannel, as described in Sect. 3.4.

(ii) Spectral unmixing

Cross-talk between the red and green channels of photodetection was removed by a linear spectral unmixing procedure. This procedure corrected for the partial overlap in emission spectra of rhodamine and fluorescein, separating the two contributions from the acquired spectrum and allowing for the calculation of the contribution of each dye to each pixel's intensity. Our procedure and its effect on the images are described in Appendix 1.

(iii) Depth-dependence compensation

The decay in the brightness of the image along the depth of the microchannel was corrected using a mathematical correction procedure. Our procedure and its effect on the images are described in Appendix 1.

(iv) Measurement of the center-of-mass of the fluorescein-labeled fluids

The center of mass of fluorescein was calculated according to the usual formula as described in the methods section. This calculation was performed on both the experimental images and the simulations, and an example of the result of these calculations is shown for the flow-rate condition $U_3/U_2 = 11$ in Figure 5. The center of mass of the experimental image was located at $x_{CM}^{EXP} = .51 \pm .02$ and $y_{CM}^{EXP} = .28 \pm .02$, as shown in Figure 5a, while the center of mass of the simulated image was located at $x_{CM}^{SIM} = .50$ and $y_{CM}^{SIM} = .27$, as shown in Figure 5b. The stated values of x_{CM} and y_{CM} are both normalized by the height, h, and width, w, of the microchannel as measured from the experimental images during the image registration procedure.

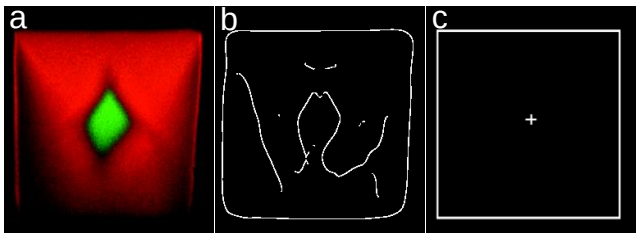

Figure 4. Image registration. a Confocal microscopy image, prior to image processing. b Result of the Sobel edge-detection operator c Rectangular approximation to the walls of the microchannel; the geometric center of the channel is shown with a *plus symbol*.

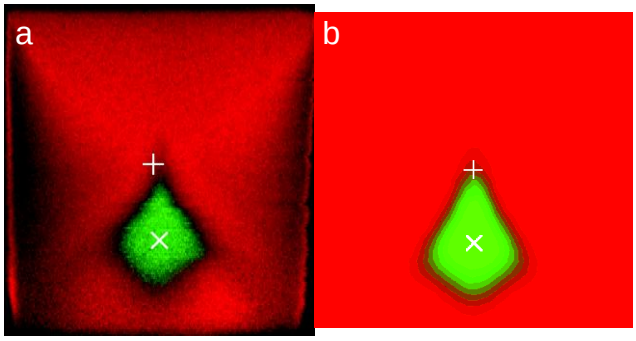

Figure 5. Fluorescence micrograph and simulation showing the center of mass of the fluorescein-labeled fluid. a Confocal microscopy image; b simulation. The geometric center of the microchannel is specified by *plus symbol* and the center of mass of the fluorescein-labeled fluids is specified by *multi symbol*.

4.4 Effect of the relative rates of the focusing fluids on the vertical position of the fluids under focusing

The experimental values of the center of mass of fluorescein, y_{CM}, are scatter-plotted against the ratio of the upper to lower focusing flow-rates, U_3/U_2, in Figure 6, and the simulations are represented by a dashed curve on the same plot. The curve representing y_{CM} according to the simulations is antisymmetric about a point-of-inflection which occurs at U_3/U_2 = 1.5. This curve decreases monotonically, more steeply near the point of inflection and leveling off at extreme values of U_3/U_2; the experimental value follow all of these trends, verifying the accuracy of our simulations. Notably, the manifold required a greater amount of focusing fluid at the upper (second) focusing input relative to the lower (first) focusing input in order to position the sample vertically at the geometric center of the microchannel; specifically, according to the simulations, $y_{CM}|_{U_3/U_2=1.5} = 0.52$ whereas $y_{CM}|_{U_3/U_2=1.0} = 0.57$.

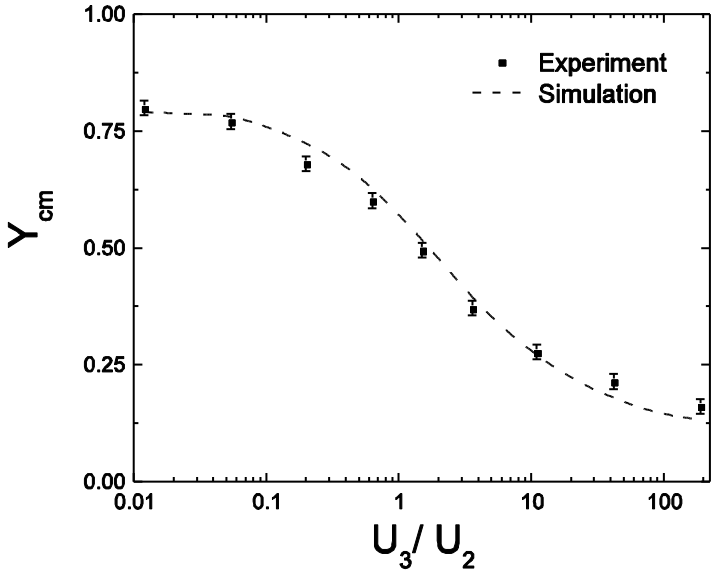

Figure 6. Effect of the ratio of the upper and lower focusing flow rates on the vertical position of the focused stream. The location of the center-of-mass of the fluorescein-labeled fluid is plotted against the ratio of the flow-rate of the upper focusing fluid to the flow-rate of lower focusing fluid, U3/U2.

5. Conclusions

A simple microlithographic hydrodynamic focusing manifold was developed which vertically steers the focused sample in a predictable manner upon adjustment to the focusing flow-rates. The movement of the sample in response to adjustments to the flow-rates was imaged with confocal microscopy and simulated with commercially available multiphysics software. Based on a simple center-of-mass measurement, the simulations accurately predicted the position of the focused stream as the ratio of the upper to lower focusing flow-rates was swept over a range of four orders of magnitude.

The manifold was fabricated by standard replica molding techniques and can be readily integrated into lab on-a-chip devices for applications. The design reduces the number of fluid inputs required to achieve three-dimensional focusing compared with previous designs (Chang et al. 2007), making this design particularly useful for the development of portable biosensors by reducing the number of required on-board fluid pumps. The manifold was designed with a feature height equal to the diameter of a standard optical fiber; therefore, using the dimensions and fabrication procedure presented in this paper, the manifold can be integrated into a microfabricated flow cytometer of the type containing imbedded optical fibers (Tung et al. 2004). In addition, the manifold and techniques described in this paper could be used to develop integrated optofluidic devices. For example, efficient coupling between solid-core waveguides and liquid-core/liquid-cladding waveguides (Wolfe, Conroy et al. 2004) should be made possible by precise steering of the high refractive index core of the fluidic waveguide. For such applications, it should be possible to steer the focused stream in both the horizontal and vertical directions (see (Nieuwenhuis, Bastemeijer et al. 2003)) by adjusting, in addition to U_3/U_2, the relative rates of the focusing fluids from the left versus the right side of the manifold.

Acknowledgements

This work was supported in part by the National Institute of Justice (NIJ #2004-DN-BX-K001) and the Ludwig Institute for Cancer Research. S.L.P. thanks the Intel Foundation and the National Nanotechnology Infrastructure Network Research Experience for Undergraduates (NNIN REU) Program. This work was performed in part at the Cornell NanoScale Facility, a member of the National Nanotechnology Infrastructure Network, which is supported by the National Science Foundation. Images were acquired at the Microscopy and Imaging Facility of the Cornell University Life Sciences Core Laboratories Center. M.J.K. thanks Anthony Reeves for discussions about the image processing and Carol Bayols for advice on the two-color imaging experiment.

APPENDIX 1

Appendix 1: Image Processing

The experimental images were modified using two image processing procedures: spectral unmixing and depth-dependence compensation. An implementation of these procedures was written in MATLAB, and a detailed discussion is provided here for the interested reader.

The net effect of image processing can be seen in Figure 7. The spectral bleedthrough of rhodamine into the green-channel is present in the original image shown in Figure 7a, but after image processing, the rhodamine appears purely red because the bleedthrough effect has been subtracted out of the processed image shown in Figure 7b. Also, the original image is brighter near the top of the microchannel than near the bottom, but the brightness of the processed image is more uniform with depth because the image has been compensated for the depth-dependent response of the optical experiment.

1. Spectral unmixing

A flat-field image was acquired in which all of the fluids pumped into the flow-cell contained rhodamine. Ideally, the rhodamine would be detected as purely red and the pixel green-values of this image would be zero everywhere. However, rhodamine was detected not only by the red-channel photodetector but also by the green-channel photodetector, and therefore the pixel green-values were non-zero and were observed to be directly proportional to the red-values. Moreover, the fraction of the red bleeding into the green depended on depth. The factor of spectral bleed-through along the depth of the channel, $F_S(y)$, was obtained by averaging the pixels horizontally and

then dividing the average green-value of each row of pixels by the average red-value of each row of pixels. It was found that $F_S(y)$ was equal to 17% near the top of the channel and 10% near the bottom of the channel.

The effect of spectral bleed-through was removed from each experimental image by subtracting the appropriate quantity from the pixel green-values according to the following formula, where I_G and I_R represent the pixel green-values and red-values of the original image and $\tilde{I}_G$ represents the pixel green-values of the unmixed image:

$$\tilde{I}_G(x,y) = I_G(x,y) - F_S(y) \cdot I_R(x,y)$$

Prior to the subtraction procedure, the pixel green-values near the top of the microchannel were brighter than the background, as shown in Figure 7c, but after the subtraction procedure, the pixel green-values were bright only in the region of the fluorescein-containing fluids, as shown in Figure 7d. This straightforward subtraction technique provides a computationally simple implementation of linear unmixing and is possible in our case because only rhodamine was detected in both the red and the green whereas fluorescein was detected only by the green-channel photodetector (Zimmermann 2005).

2. Depth-dependence compensation

Depth-dependence compensation was required because the original images were bright near the top of the microchannel and dim near the bottom of the microchannel. This depth-dependence of image brightness did not reflect the concentration distributions of the fluids but resulted from uneven illumination along the depth of the specimen and imperfections of the optical detection system of the microscope.

The spatial decay of light intensity with depth has been encountered previously in 3-D confocal microscopy, and two competing methods have been used to correct this

decay: image arithmetic and mathematical correction. The image arithmetic approach normalizes the images according to a formula originally developed for fluorescence microscopy (Park, Kim et al. 2004):

$$CI = \frac{OI - DF}{FF - DF},$$

where OI represents the original image, CI represents the corrected image, DF represents the dark-field image in which no dye is present, and FF represents the flat-field image in which dye is uniformly present. This technique relies heavily on the precise alignment of the dark-field image to the flat-field and experimental images. In practice, however, it can be difficult to register the dark-field image to the experimental images because the walls of the channel cannot be detected in the absence of fluorescently dyed fluids. For this reason, we elected to restore the images using a mathematical correction method.

Several alternative mathematical correction methods have been developed to correct confocal microscopy images suffering from the effect of depth-decay of brightness (Umesh Adiga and Chaudhuri 2000). Seeking ease of computation, we have developed a simple method of correction based on a linear fit and linear transformation. Our procedure begins by describing the decay of fluorescence intensity with depth based on the flat-field images. Two flat-field images were obtained: first, all of the inputs to the flow-cell were loaded with rhodamine and a red flat-field image was acquired, I_R^{FF} ; second, all of the fluid inputs to the flow-cell were loaded with fluorescein and a green flat-field image was acquired, I_G^{FF} . An horizontal median filter was applied to the flat-field image in which fluorescein-labeled fluid was pumped into all of the inputs of the flow-cell using the *nlfilter()* function of MATLAB with a sliding block of 20x1 pixels. Then, a profile was obtained vertically up the center, revealing a profile of the depth-dependence of the intensity of fluorescence,

$I_G^{FF}(y)$. The parameters describing the depth-dependence were obtained by fitting this profile with the following equation:

$$I_G^{FF}(y_C - y)|_{y<y_C} = m_G \cdot (y_C - y) + b_G$$
$$I_G^{FF}(y_C)|_{y>y_C} = b_G$$

where a characteristic height was identified, y_C, above which the image brightness was approximately constant and below which the brightness decayed approximately linearly, and where the fitting parameters m_G and b_G were obtained by linear regression. For the green flat-field image, $I_G^{FF}(x,y)$, this decay occurred for $y < y_G^C$, where $y_G^C = 0.63$ and y is measured from the bottom of the channel is normalized to one at the top of the channel. The slope of decay was m_R = -1.9 ± 0.1 μm^{-1}, and the intercept at y_G was b_G = 217 ± 3; here, it is useful to recall that the pixel-values of the original image were 8-bit integers ranging from 0 to 255. The fitting procedure was repeadted similarly for the red flat-field image, $I_R^{FF}(x,y)$, and it was found in this case that $y_R^C = .49$, m_R = -1.9 ± 0.1 μm^{-1}, and $b_R = 213 \pm 9$.

With these parameters at hand, each experimental image was restored of depth decay by applying the following transformation independently to the red color-component of the image, $I_R(x,y)$, and the green color-component of the image, $I_G(x,y)$, where $I'(x,y)$ is the corrected image:

$$I'(x,y) = I(x,y) \cdot \frac{b}{m \cdot y + b}.$$

Prior to the procedure, the red pixel-values were less bright near the bottom of the microchannel than the top in the original image, as shown in Figure 7e, but after the procedure, the red pixel-values near the top and bottom of the microchannel were of similar brightness, as shown in Figure 7f.

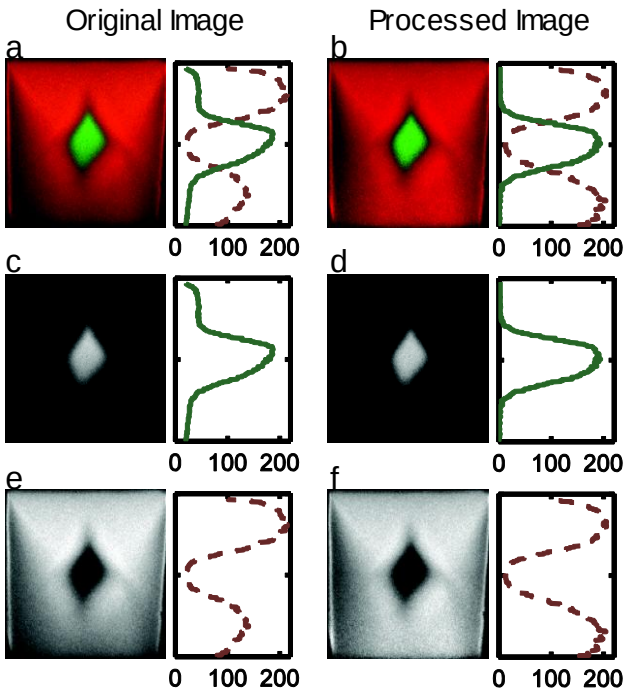

Figure 7. Fluorescence micrographs and intensity profiles showing the effect of image processing. a Original image alongside a profile of the pixel green-values (solid line) and pixel red-values (dashed line) obtained along the vertical center of the image. The image pixels contained integer values between 0 and 255. In each of the pixel profiles, y varies along the vertical axis from y = 0 to y = 1. b Processed image; c original image, pixel green-values; d processed image, pixel green-values; e original image, pixel red-values; f processed image, pixel red-values.

REFERENCE

Chang, C.-C., Z.-X. Huang, et al. (2007). "Three-dimensional hydrodynamic focusing in two-layer polydimethylsiloxane microchannels." Journal of Micromechanics and Microengineering **17**(8): 1479-1486.

Dickinson, M. E., G. Bearman, et al. (2001). "Multi-spectral imaging and linear unmixing add a whole new dimension to laser scanning fluorescence microscopy." Biotechniques **31**(6): 1272-1278.

Fu, L.-M., R.-J. Yang, et al. (2004). "Electrokinetically driven micro flow cytometers with integrated fiber optics for on-line cell/particle detection." Analytica Chimica Acta **507**(1): 163-169.

Goddard, G. R., C. K. Sanders, et al. (2007). "Analytical Performance of an Ultrasonic Particle Focusing Flow Cytometer." Analytical Chemistry **79**(22): 8740-8746.

Holmes, D., H. Morgan, et al. (2006). "High throughput particle analysis: Combining dielectrophoretic particle focussing with confocal optical detection." Biosensors and Bioelectronics **21**(8): 1621-1630.

Knight, J. B., A. Vishwanath, et al. (1998). "Hydrodynamic Focusing on a Silicon Chip: Mixing Nanoliters in Microseconds." Physical Review Letters **80**(17): 3863.

Kohlheyer, D., S. Unnikrishnan, et al. (2008). "A microfluidic device for array patterning by perpendicular electrokinetic focusing." Microfluidics and Nanofluidics **4**(6): 557-564.

Laulicht, B., P. Cheifetz, et al. (2008). "Evaluation of Continuous Flow Nanosphere Formation by Controlled Microfluidic Transport." Langmuir **24**(17): 9717-9726.

McClain, M. A., C. T. Culbertson, et al. (2001). "Flow Cytometry of Escherichia coli on Microfluidic Devices." Analytical Chemistry **73**(21): 5334-5338.

Nieuwenhuis, J. H., J. Bastemeijer, et al. (2003). "Integrated flow-cells for novel

adjustable sheath flows." Lab Chip **3**(2): 56-61.

Park, S. J., J. K. Kim, et al. (2004). "Rapid three-dimensional passive rotation micromixer using the breakup process." Journal of Micromechanics and Microengineering **14**(1): 6-14.

Pollack, L., M. W. Tate, et al. (2001). "Time Resolved Collapse of a Folding Protein Observed with Small Angle X-Ray Scattering." Physical Review Letters **86**(21): 4962.

Shin, S.-J., J.-Y. Park, et al. (2007). "On the Fly Continuous Generation of Alginate Fibers Using a Microfluidic Device." Langmuir **23**(17): 9104-9108.

Simonnet, C. and A. Groisman (2005). "Two-dimensional hydrodynamic focusing in a simple microfluidic device." Applied Physics Letters **87**(11): 114104.

Sundararajan, N., M. S. Pio, et al. (2004). "Three-dimensional hydrodynamic focusing in polydimethylsiloxane (PDMS) microchannels." Microelectromechanical Systems, Journal of **13**(4): 559-567.

Tung, Y.-C., M. Zhang, et al. (2004). "PDMS-based opto-fluidic micro flow cytometer with two-color, multi-angle fluorescence detection capability using PIN photodiodes." Sensors and Actuators B: Chemical **98**(2-3): 356-367.

Umesh Adiga, P. S. and B. B. Chaudhuri (2000). "Some efficient methods to correct confocal images for easy interpretation." Micron **32**(4): 363-370.

Wang, Z., J. El-Ali, et al. (2004). Microchip flow cytometer with integrated polymer optical elements for measurement of scattered light. Micro Electro Mechanical Systems, 2004. 17th IEEE International Conference on. (MEMS).

Wolfe, D. B., R. S. Conroy, et al. (2004). "Dynamic control of liquid-core/liquid-cladding optical waveguides." Proceedings of the National Academy of Sciences of the USA **101**(34): 12434-12438.

Zhao, Y., B. S. Fujimoto, et al. (2007). "Optical gradient flow focusing." Optics Express **15**(10): 6167-6176.

Zimmermann, T. (2005). Spectral Imaging and Linear Unmixing in Light Microscopy. Microscopy Techniques**:** 245-265.

CHAPTER 2

MICRO- FLOW CYTOMETER WITH HYDRODYNAMIC OPTICAL ALIGNMENT

ABSTRACT

A micro-flow cytometer is presented in which the optical alignment between the particle stream and the fixed illuminating beam was adjusted hydrodynamically via the flow-rates of the focusing fluids. Inthe present device, the optics were coupled to the microfluidic channel via imbedded optical fibers. The particle-stream was maneuvered up and down by adjusting the focusing flow-rates, and when the particle stream was aligned with the laser the maximum absolute counting efficiency was 58±8% for fluorescent microparticles injected at a volumetric throughput of 5.5 μL/min along with sheath fluid at 49.5 μL/min. The typical coefficient of variation (CV) of the fluorescent pulse-heights using 632.8 nm excitation was 15% for the micro-flow cytometer compared with 6% for a commercial instrument.

1. Introduction

Cytometers are immobile instruments used in clinical and research laboratories, and most require dedicated personnel for operation and maintenance. Using lab-on-a-chip technology, it should be possible to develop portable cytometers that can be operated at the point-of-detection by minimally trained personnel. This is important for pathogen detection, environmental microbiology, and for the treatment of AIDS in rural parts of the world. At this time, microflow cytometers have been demonstrated in research laboratory settings for the analysis of bead-based immunoassays (Yang, Lien et al. 2008; Kim, Anderson et al. 2009) and for the identification of subpopulations of blood cells in blood (Kummrow, Theisen et al. 2009).

Microfluidics reduces the volume of sample that is required and also the volume of hazardous fluid waste that is produced. Unlike the cuvettes used in conventional

cytometers, microfluidic devices are compatible with large-scale manufacturing methods. Therefore, the potential exists to manufacture disposable cytometer cartridges, allowing a fresh device to be used for each test analogous to the i-STAT, an electrochemical based point-of-care biosensor that is finding increased use in clinical settings.

Microfluidic devices can constructed to embody imbedded micro-optical components such as waveguides, optical fibers, and fiber-to-waveguide couplers (Wang, El-Ali et al. 2004). Importantly, imbedded optics results in high shock-stability compared with free-space optical systems, which is useful for portability. Conventionally, flow cytometer optical detection systems have been large in size due to their reliance on free-space optics and the accompanying mechanical micropositioning equipment. Several groups have taken steps towards eliminating this micropositioning equipment by constructing micro-flow cytometers with imbedded optical fibers (Fu, Yang et al. 2004; Tung, Zhang et al. 2004; Wang, El-Ali et al. 2004). In these systems, imbedded optical fibers results in simplified removal and replacement of the microfabricated device from the supporting apparatus. Specifically, upon discarding the old device, the fibers protruding from the new device can be attached to the supporting apparatus using twist-and-lock connections.

Microfluidic focusing devices confine a suspension into a subregion of the microfluidic channel. Three-dimensional focusing devices, which focus a suspension in a cylindrical lamina[1], have been used in optical fiber-based micro- flow cytometers in order to prevent the partical stream from traveling either above or below the in-plane illuminating beam (Golden, Kim et al. 2009; Kummrow, Theisen et al. 2009).

[1] Strictly speaking, this type of focusing acts in only two dimensions, however in practice the microfluidics community has referred this as three-dimensional focusing.

Three-dimensional focusing has been accomplished hydrodynamically using bas-relief structures (Golden, Kim et al. 2009), microfluidic drifting (Mao, Lin et al. 2009), and multi-layer junctions (Chang, Huang et al. 2007; Kennedy, Stelick et al. 2009). An advantage of the multi-layer junctions-based devices is their ability to adjust, on-the-fly, the vertical position of the particle stream (Kennedy, Stelick et al. 2009). In addition to hydrodynamics-based focusing, alternative techniques have been used for three-dimensional focusing such as dielectrophoresis (Holmes, Morgan et al. 2006).

In the present work, a microflow cytometer is described which integrates a three-dimensional hydrodynamic focusing manifold and an optical fiber-based detection system similar to Golden et al. (Golden, Kim et al. 2009) but which allows for the optical alignment to be adjusted hydrodynamically via the flow-rates of the focusing fluids.

2. Methods

2.1 Description of the device

The device layout included two components: the hydrodynamic focusing manifold and the integrated optics, as illustrated in Figure 8. The hydrodynamic focusing manifold comprised a two-layer structure that impinged the suspension-under-focusing first from below and then from above by fluids from the adjoining layer. The suspension-under-focusing was injected at volumetric flow-rate U_1, and the upper and lower focusing fluids were injected at rates U_2 and U_3, respectively. The total volumetric flow-rate was kept fixed at $U_{TOT} = U_1 + 2U_2 + 2U_3$. The three independent flow-rates, U_1, U_2, and U_3, were driven by three syringe pumps (PHD 2000, Harvard Instruments) using disposable syringes. In the present study, the volume of the suspension-under-focusing as a fraction of total fluid volume was fixed as $U_1/U_{TOT} = 1/10$.

The device was fabricated in the Cornell Nanofabrication Facility according to the methods explained in detail in our previous work (Kennedy, Stelick et al. 2009). The feature height of the microfluidic channels was chosen to be 125 μm, which corresponds to the diameter of a standard optical fiber. Briefly, polydimethylsiloxane pieces were replica-molded from a silicon master, which was created by patterning SU-8 polyimide resist (Microchem) on a silicon wafer using photolithography. Two masters were used, and complementary pieces of PDMS were pealed from each of these two masters, exposed to a 200-W oxygen plasma for 20-seconds, and then brought into aligned contact using a contact aligner.

Optical fiber insertion guides were included in the microfluidic layout at dead-end distances of approximately 50 μm from the edge of the fluid channel. After fabrication of the microfluidic chip, optical fibers were sheath-stripped and cleaved and then inserted into the fiber insertion guides. Optical adhesive was used to permanently fix the fibers into place (Norland Optical Adhesive #63).

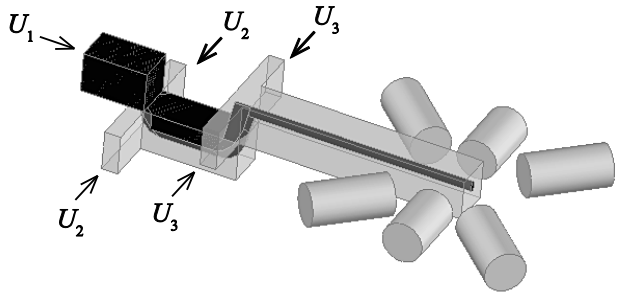

Figure 8. Illustration shows the three-dimensional hydrodynamic focusing manifold leading into an optical fiber-based interrogation zone. The beads were injected at volumetric flow-rate U_1, which in the present study was fixed at 1/10 the total volumetric flow-rate, U_{TOT}. The lower and upper focusing fluids were injected at rates U_2 and U_3, respectively, such that the total volumetric flow-rate was equal to $U_{TOT} = U_1 + 2U_2+2U_3$.

2.2 Optical detection system

A 5-mW 633-nm HeNe Laser was used as an excitation source, and this illumination was delivered with the microfluidic channel at an angle of 90º using a single-mode fiber with a cutoff wavelength of 500-600 nm (F-SV, Newport). A total of three signals were simultaneously acquired using three identical PMTs (H5784, Hamamatsu, Japan): side-scatter at 45º (SS 45), side-scatter at 135º (SS 135), and fluorescence at 660/30 (660/30). Multimode fibers were used for the collection of fluorescence and scattered radiation. A bright-field micrograph shows the optical interrogation zone marked-up with a schematic representation of the optical detection system in Figure 9.

Electronic power supplies were constructed in-house, which supplied source voltages to the PMTs using DC-DC converters (DKE10A-15, Mean-well, USA). The control voltage, *i.e.* gain, applied to each PMT was tuned between 0V and 1V using a resistive voltage divider, and this gain was monitored using a panel LED voltage monitor (DMS-20LCD-1-5-C, Murata Power Solutions).

Data was acquired by recording signals from the photomultiplier tubes (PMTs) using a multi-channel digital oscilloscope (WaveRunner 6050, LeCroy). The entrance of each PMT was fixed to a collimation tube, which was fitted with an adaptor for connecting an optical fiber. The collimation tubes contained the necessary optical filters for each signal. Specifically, the entrance to the fluorescence detector was filtered using a 660/30 bandpass filter and a 632 nm notch filter (Chroma, USA), and the scattering detectors were filtered using 632/10 bandpass filters (Thorlabs). Note that six fibers were imbedded in the device, but only four of these were used in the present study. Therefore, it would be straightforward to add an additional photodetector for the quantification of a fluorescein-labeled target, a technique which has been used previously for multiplexed bead-based assays.

Oscilloscope traces were acquired and saved as individual binary oscilloscope files onto an external hard disk drive. Waveform collection was triggered on SS 45 using AC coupling, and SS 135 and 660/30 were acquired simultaneously with SS 45 using DC coupling. After data collection was complete, the waveforms were digitally processed using a matlab script. The script first low-pass-filtered all three signals using a time-domain mean filter with an integration time in the range of 1-50 μs, which depended on the flow-rate with shorter integration times used at higher flow-rates. Then, the script thresholded the SS 45 signal at 4 standard deviations above baseline. The time-difference between the two threshold-crossing points yielded the pulse-duration, the local maximum of the low-pass-filtered signal between these two points yielded the pulse-height, and the area under the waveform integrated between these points yielded the pulse-area. The script processeda large number of waveforms, parameterized the photon-burst events in terms of pulse-duration, pulse-height, and pulse-area, and recorded these quantities in a text file that served as a parameterized list of events.

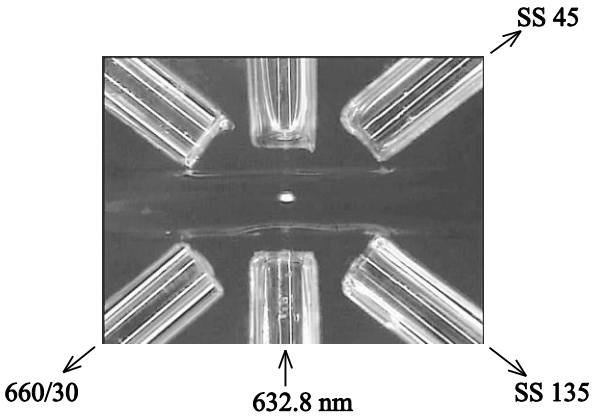

Figure 9. Brightfield micrograph shows the optical interrogation zone of the micro-flow cytometer. The fluorescent bead shown passing through the illuminating beam was 6 μm in diameter. The width of the microchannel and the diameter of the optical fibers were each 125 μm. Scattered radiation was collected at angles of 45º and 135º, and fluorescence was collected at 660 nm with a bandwidth of 30 nm.

2.3 Materials and reagents

The focusing solution consisted of 2 mM potassium phosphate monobasic, 16.6 mM sodium phosphate dibasic, 3.8 mM potassium chloride, and 139 mM sodium chloride, adjusted to pH 7.4, with 0.05% tween20 added. The focusing solution was stored at 5X concentration, without tween, to inhibit contamination by yeast, and was diluted to its working concentration prior to the experiment. The bead suspension buffer consisted of focusing solution with 30% polyethylene glycol added, MW = 3350. The purpose of adding the polyethylene glycol was to prevent the beads from settling out of solution onto the bottom of the syringe by matching the density of the solution to that of the beads. The focusing solution was autoclaved for 15 minutes and cooled in the refrigerator prior to experiment in order to remove trapped gases from the buffer thereby mitigating the formation of bubbles inside the microfluidic device.

Intensity calibration beads specific for 633 nm excitation and 660 nm emission were purchased from Invitrogen (LinearFlow^{TM} Deep Red Flow Cytometry Intensity Calibration Kit). The intensity calibration kit contained six bead-sets, packaged in individual containers, each at a common concentration of 1.8 x 10^7/mL according to the manufacturer specifications. The LinearFlow^{TM} beads were 6 μm in diameter. Of the six sets of beads, the particular set with the highest fluorescence intensity was analyzed along with absolute counting microspheres at the Cornell Core Flow Cytometry Facility on a commercial flow cytometer instrument (LSR II, Becton Dickinson), and the measured bead concentration was 1.5 x 10^7/mL. Therefore, the absolute concentration of this set of microspheres, which was used in the measurements of absolute counting efficiency, was assumed to be the average of these two measurements, *i.e.* 1.7±0.2 x 10^7/mL.

3. Results

3.1 Hydrodynamic alignment of the bead stream with the optical detection system

A 50X dilution of the brightest subset of beads from the LinearFlow™ Intensity Calibration Kit, corresponding to a concentration of 3.3±0.4 x 10^5/mL, was injected into the micro- flow cytometer at four different volumetric flow-rates, which are listed in Table 1. At each volumetric flow-rate, the ratio of upper focusing fluid to lower focusing fluid was adjusted in steps from U_3/U_2 = 126 to U_3/U_2 = 0.012, which corresponded to the suspension-under-focusing being positioned first at the bottom of the microchannel and then translated upwards to the top. At each step in U_3/U_2, more than one-hundred waveforms were collected. In order to measure absolute counting efficiency, the triggering threshold on the oscilloscope was set sufficiently low to trigger the waveforms on random noise, and waveforms were acquired that were long compared with the duration of a single pulse such that when the bead stream was aligned with the laser beam, several events were collected per waveform. In this way, 100 waveforms collectively contained more than 1,000 thresholded events. The waveforms were collected at rates of digitization of 1 MHz or higher, with higher rates of digitization used at higher rates of flow. The waveforms were processed digitally yielding a parameterized list of events, as explained in the methods section. The parameterized events were gated from the scatter-plot of 660/30 vs SS 135 in order to eliminate bad events that did not fall within the cluster corresponding to the particular beads under analysis. The number of gated events was compared with the known rate of bead throughput yielding the absolute counting efficiency.

The maximum absolute counting efficiency was 58±8%, which was observed at a focusing ratio of U_3/U_2 = 0.40 with the device operated at u_{AVG} = 5.9 cm/s (Figure 10). At higher flow-rates, optimized absolute counting efficiency required increased fractions of upper- relative to lower- focusing fluid. Specifically, whereas counting

efficiency was optimized at U_3/U_2 = 0.40 for operation at mean fluid-velocities in the range of u_{AVG} = 2-16 cm/s, the counting efficiency was optimized instead at U_3/U_2 = 1.0 for operation at u_{AVG} = 44 cm/s. Importantly, this shift in the focusing ratio does not indicate a vertical migration of the optical beam but rather a change in the hydrodynamics at higher fluid velocities. At higher fluid velocities, a greater quantity of focusing fluid was needed at the second stage of focusing in order to push the bead-suspension downwards into the illuminating beam.

Notably, a single 3 mL bead suspension was used to acquire all of the data points in Figure 10, and all of this data was acquired during one continuous operation on one day. A limited number of data points were acquired at the highest rate of flow because towards the end of data acquisition, the syringe became empty. The maximum absolute counting efficiency was observed to decrease at higher rates of flow. Notably, the PMT-gains were held at a fixed voltage for the duration of the experiment. It is conceivable that increasing the PMT-gains as the flow-rate is increased could mitigate the trend of decreasing counting efficiency at higher rates of flow.

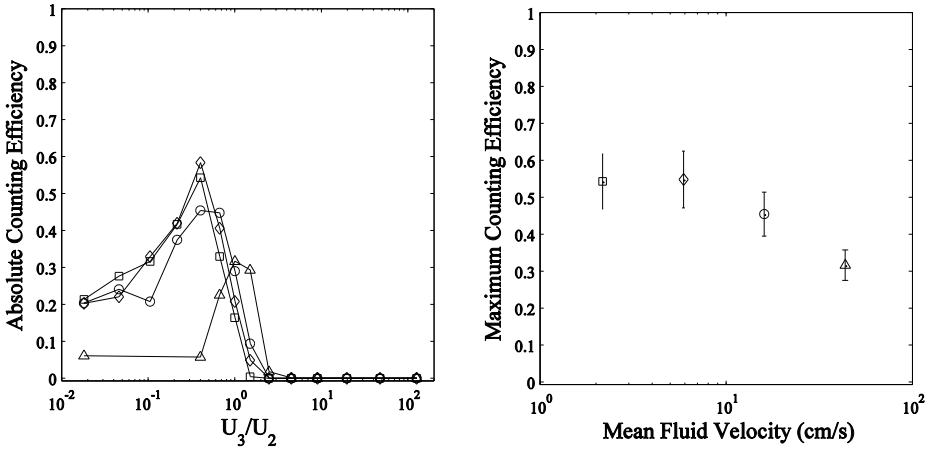

Figure 10. Absolute counting of fluorescent microspheres. (Left) Plot shows the absolute counting efficiency of far-red fluorescent microspheres versus the ratio of the upper and lower focusing fluids, U_3/U_2. Data was acquired at fluid velocities of u_{AVG} = 2.2 cm/s (□), 5.9 cm/s (◊), 16 cm/s (○), and 44 cm/s (Δ). (Right) Plot shows the local maximum achieved for each fluid velocity, from left, along with an indication of the error of the measurement of maximum absolute counting efficiency.

Table 1. List shows the volumetric flow-rates and the corresponding Reynolds numbers and mean fluid velocities under which the device was operated.

Mean fluid velocity (cm/s)	2.2	5.9	16	44
Volumetric flow-rate (μL/min)	20	55	150	410
Reynolds number	2.7	7.4	20	55

3.2 Multiplexed detection of microspheres of different fluorescence intensities

Intensity calibration beads with 6 relative median fluorescence intensities (MFIs) ranging from .05% to 100% were added to a common bead-suspension and injected such that the mean fluid-velocity was u_{AVG} = 2.2 cm/s. Waveforms of 10-ms duration were collected at a 200-MHz rate of digitization by triggering on SS 45. A total of 1,000 sets of waveforms were collected. Typical pulses were about 1 ms in duration.

Scatterplots of 660/30 vs. SS 45 reveal a direct correlation between scattering intensity and fluorescence. This occurred due to the intensity profile of the illuminating beam: beads passing through center of the beam scattered more light and also emitted more fluorescence than beads passing through the edge of the beam. To remove this effect, the fluorescence pulse-areas and also the scattering pulse-areas were each normalized by the respective pulse-durations, and then the resulting normalized fluorescence pulses were further normalized by the normalized scattering pulses, following Golden et al. (Golden, Kim et al. 2009). The result of this transformation is shown in Figure 11. Up to four subpopulations of microspheres could be distinguished from one another based on fluorescence intensity. Of the six populations, the faintest three populations could not be distinguished from another. Most events from the faintest two populations occurred within the noise floor of the signal, and during the normalization procedure many of these events were transformed into the gate for the fourth population. The dynamic range of the detection system was limited to 2.4 logs because the oscilloscope used an 8-bit analog-to-digital converter. The dynamic range was increased slightly beyond 8 bits post- data acquisition by the digital integration procedure (low-pass-filtering). In a future system, it should be possible to achieve greater dynamic range and to distinguish a larger number of populations by using a higher-resolution analog-to-digital converter.

The four populations of greatest fluorescence intensity were fit with CVs of 15%,

15%, 17%, and 35%, assuming a normal distribution about their MFIs. The bead mixture was analyzed for comparison on a commercial cytometer instrument (LSR II, Becton Dickinson), and these four populations were fit with CVs of 7%, 5%, 6%, and 6%. Notably, the CVs reported in the present study are greater than those that have been reported in some previous studies due to our use of far-red microspheres with excitation from a 633-nm source as opposed to green microspheres with excitation from a 488-nm source. The distributions of fluorescence intensity for the two cytometers are compared in Figure 12. The values for the MFI, CV, and the number of events in each gate, are listed in Table 2.

The micro-flow cytometer exhibited a linear response over a range of 2.2 logs as verified by comparing the MFIs measured using the micro- flow cytometer and measured using the commercial instrument. A linear model was fit through the pairs of data-points for the three beads of greatest fluorescence intensity, and this fit was extended to that of the fourth bead. The root-mean-squared-relative error between the linear model and the data points was 1.8%. For the first three data points, the root-mean-squared-relative-error was less than 0.1% whereas for the last data point the relative error was 7%. It can be concluded that the response was strongly linear over the first 1.6 logs of dynamic range and weakly linear over the remaining 0.6 logs. The linearity can be extended to a greater range by using a higher-resolution analog-to-digital converter.

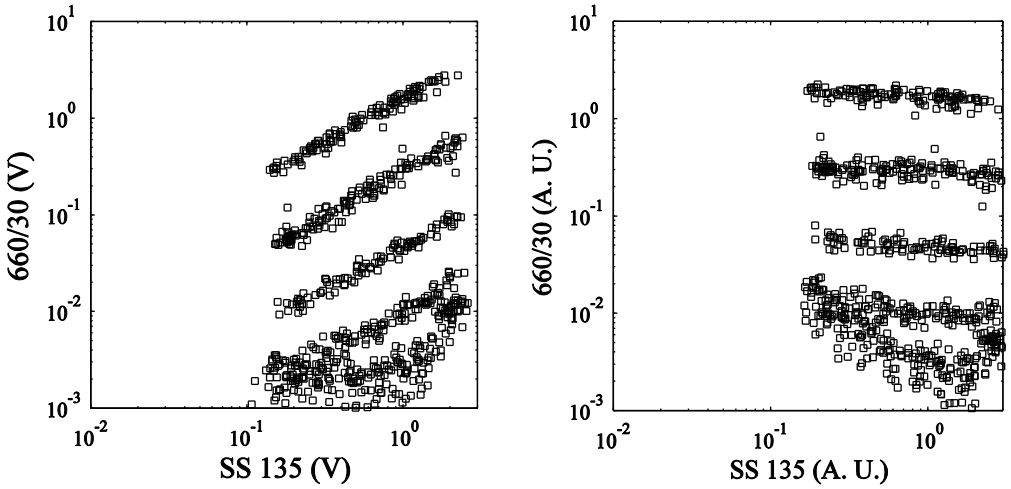

Figure 11: Scatterplots show the effect of the normalization procedure in which the fluorescence pulse-heights are normalized by the scattering pulse-heights. Left: Scatterplot shows the fluorescence pulse-heights verses the scattering pulse-heights, as acquired using a digital oscilloscope, for a suspension containing 6 populations of fluorescence intensity standard calibration beads. Right: Scatterplot shows the normalized fluorescence pulse-heights verses the scattering pulse-heights. The original pulse-heights are in units of volts (V), and the normalized pulse-heights are in arbitrary units (A. U.).

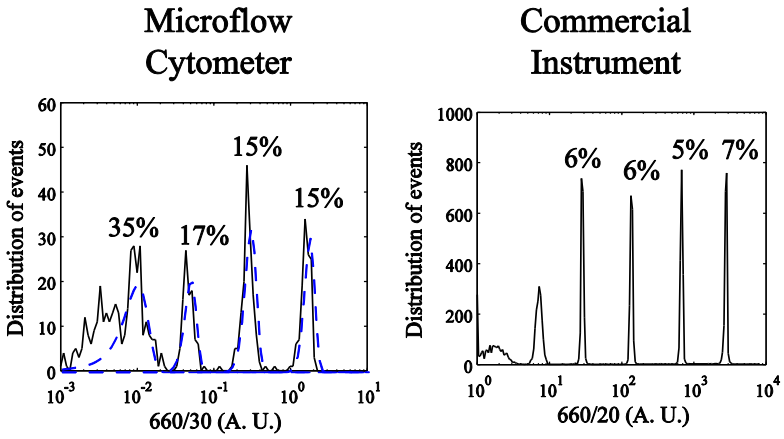

Figure 12. Histograms show the fluorescence intensity response for a mixture of linear intensity standard calibration microspheres analyzed using the microflow cytometer (Left) and, for comparison, using a commercial instrument (Right). Dashed curves show analytical fits according to the normal distribution. The left histogram shows a total of 600 events, and the right histogram shows a total of 10,000 events.

Table 2. List shows the median fluorescence intensity, coefficient of variation, and number of gated events (N) for the brightest four subsets of beads from the fluorescence intensity standard calibration kit, as measured using the micro- flow cytometer and as measured using the commercial instrument (LSR II, Becton Dickinson, USA).

	Bead 1	Bead 2	Bead 3	Bead 4
Micro- flow cytometer				
MFI	100%	17%	2.8%	0.57%
CV	15%	17%	17%	35%
N	123	149	98	215
Comercial Instrumnet				
MFI	100%	24%	4.6%	0.92%
CV	7%	6%	6%	6%
N	1,717	1,633	1,643	1,797

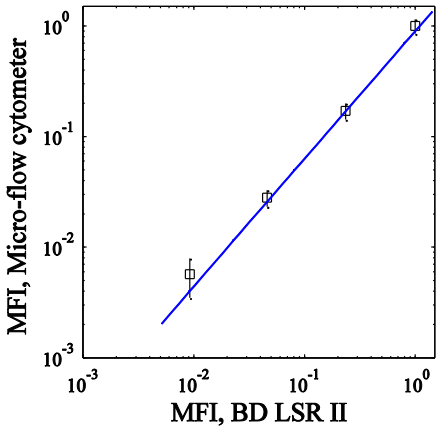

Figure 13. Linearity of the fluorescence response of the micro-flow cytometer. Plot shows the relative MFIs of the four subpopulations of greatest fluorescence intensity from the linear intensity standard calibration kit, as measured using the commercial flow cytometer (x-axis) and as measured using the micro- flow cytometer (y-axis). Curve shows a linear regression model fit through the right-most three points and extended to the left-most point. Error bars represent the CV of each distribution.

3.3 Effect of hydrodynamic alignment on spectral resolution

Fluorescence pulse-height distributions were acquired for a range of U_3/U_2, yielding histograms similar to that shown previously in Figure 12, which was acquired specifically at $U_3/U_2 = 1.0$. The typical CV at each ratio of the upper to lower focusing fluids was measured by averaging the CVs corresponding to the two sets of beads of greatest fluorescence intensity. Distributions were acquired between $U_3/U_2 = 0.012$ and $U_3/U_2 = 1.5$, and these data are plotted in Figure 14. For focusing ratios $U_3/U_2 > 1.5$, data could not be collected due to a lack of photon-burst events resulting from poor hydrodynamic alignment between the bead stream and the laser beam. Tellingly, the CV was minimized by aligning the bead stream not necessarily with the center of the laser beam but with the center of the microfluidic channel. This indicates that the spectral resolution, as measured by the CV of the normalized fluorescence pulse-heights, may be limited not by the optics but by the hydrodynamics. Only one previous study reported a CV for an optical fiber-based micro-flow cytometer. Specifically, Golden et al. reported a typical CV of 15% for fluorescently labeled particles from a bead-based assay. Our results agree with those of Golden et al., however, it is important to note that this agreement may result from coincidentally similar velocity distributions achieved by two distinct hydrodynamic focusing techniques and not simply from the similarity in the two optical detection systems. In order to reduce the CV to less than 15% in the present device, the hydrodynamic focusing should be improved by redesign with a strong emphasis on the minimization of any variation in the velocity-distribution of the suspension-under-focusing. According to multiphysics simulations, when the suspension-under-focusing is aligned with the center of the microfluidic channel, its velocity distribution varies by 7% (data not shown).

It is known that 3-D focusing in micro-flow cytometers reduces the coefficient of

variation (CV) of the fluorescence pulses, and micro-flow cytometers have been demonstrated using digital data acquisition electronics similar to those used in the present study with CVs approximately equal to those obtained using commercial instruments (3%-5%) using free-space optics (Simonnet and Groisman 2006). Therefore, in the present study the spectral resolution did not approach the limits which have been achieved previously in free space optics-based micro- flow cytometers, and at this time it is not known how much of the 15% variation observed in the present study was due to the fiber-based detection system verses imperfect hydrodynamic focusing. In one study, Kummrow et al. analyzed a microfluidic device using both optical fibers and free-space optics. While CV measurements were reported only for the free-space optics system, it was reported that the pulse-height distributions were narrower using free-space-optics compared with the optical-fibers (Kummrow, Theisen et al. 2009). At this time, it remains unclear whether micro-optics will come to rival free-space optics for flow cytometry with regard to spectral resolution.

The optical detection zone can be visualized by examining the diameter of the illuminating beam. Specifically, the mean pulse-duration was .82 ±.08 ms for SS 45 pulses as measured according to the threshold-crossings at 4 standard deviations above baseline when the device was operated at a mean fluid velocity of u_{AVG} = 2.2 cm/s. Assuming the beads were traveling at the mean fluid velocity, the beam waist was 18 µm.[2] A histogram shows the durations of the SS 45 pulses in Figure 15. The

[2] In the field of optics, the beam waist is commonly measured according to its full-width at half-max (FWHM). In the present work, the FWHM of the SS 45 signal was equal to approximately 1/2 the pulse-width as according to the threshold-crossing points. Therefore, the mode-field diameter of the illuminating beam at the location of excitation was approximately 9 µm.

durations were similar for the SS 135 signal and 660/30. Importantly, the measured beam waist was smaller than the vertical height of the bead stream. Specifically, the bead stream according to simulations was approximately 20 um in width and 40 um in height (Kennedy, Stelick et al. 2009). Therefore, it should be possible to increase the absolute counting efficiency beyond 58% by focusing the bead suspension into a smaller lamina.

Multiphysics simulations indicate that maximum counting efficiency occurred not when the bead suspension was located in the geometric center of the mirochannel, but when it was displaced vertically upwards by 15% of the microchannel height, or 20 μm, with its vertical center-of-mass located at y_{CM} = 0.65 (Kennedy, Stelick et al. 2009). Based on this analysis, it can be concluded that the imbedded optical fiber used for guiding the laser into the device was not aligned with the vertical center of the microchannel. This misalignment is a fabrication issue and can be resolved in future devices.

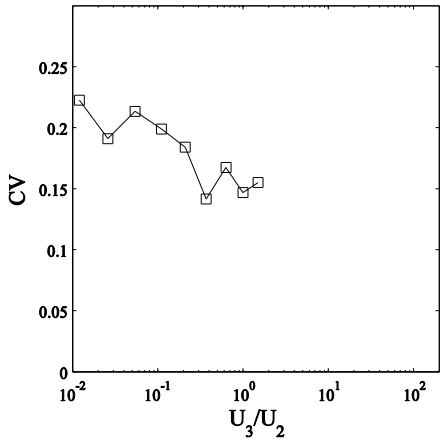

Figure 14: Plot shows the coefficient of variation of the pulse-heights for fluorescent microparticles versus the ratio of the upper and lower focusing fluids. The mean fluid-velocity was u_{AVG} = 2.2 cm/s.

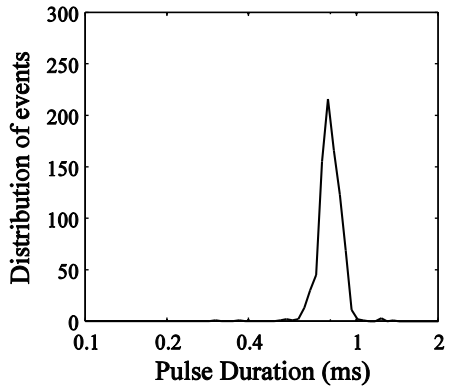

Figure 15: Histogram shows the distribution of the durations of the pulses for operation at u_{AVG} = 2.2 cm/s, U_3/U_2 = 0.40, as measured according to the threshold-crossings of SS 45 signal at 4 standard deviations above baseline. Based on the mean pulse duration from this histogram, 0.82 ms, the diameter of the illuminating beam was 18 μm at the location of optical excitation.

4. Conclusions

When the hydrodynamic alignment between the bead stream and the laser was optimized, the device counted more than half the particles under focusing. It may be possible to increase the absolute counting efficiency beyond this quantity by focusing the bead stream into a tighter subregion of the microfluidic channel.

Absolute counting efficiency and spectral resolution could not be optimized simultaneously since, due to fabrication issues, the location of the illuminating beam did not coincide with the center of the microchannel. In future optical fiber-based micro-flow cytometers, it is important that the illuminating beam be guided as close as possible to the geometric center of the microfluidic channel.

The measurement of the CV of the fluorescence pulse-height distributions in the present study agreed with the previously reported value for an optical fiber-based cytometer, *i.e.* CV ~ 15% (Golden et al. 2009). However, this value may not represent the limitation of fiber-optics-based illumination. Rather, it appears that the hydrodynamic variation in the velocities of the beads may have contributed significantly to this variation. Therefore, it should be possible to reduce the CV to less than 15% by improving the hydrodynamic focusing, assuming the variation of the velocity-distribution of the suspension-under-focusing can be reduced in this manner. In the future, the design of microfluidic hydrodynamic focusing devices for flow cytometry should minimize any variation in the velocity-distribution of the suspension-under-focusing.

At this time the present technology can distinguish the fluorescence signatures from beads of varying fluorescence intensity. By adding a second laser, the present device can be used to analyze a multiplexed bead-based assay similar to (Kim, Anderson et al. 2009).

REFERENCE

Chang, C.-C., Z.-X. Huang, et al. (2007). "Three-dimensional hydrodynamic focusing in two-layer polydimethylsiloxane (PDMS) microchannels." Journal of Micromechanics and Microengineering **17**: 1479-1486.

Fu, L.-M., R.-J. Yang, et al. (2004). "Electrokinetically driven micro flow cytometers with integrated fiber optics for on-line cell/particle detection." Analytica Chimica Acta **507**(1): 163-169.

Golden, J. P., J. S. Kim, et al. (2009). "Multi-wavelength microflow cytometer using groove-generated sheath flow." Lab on a Chip **9**: 1942-1950.

Holmes, D., H. Morgan, et al. (2006). "High throughput particle analysis: Combining dielectrophoretic particle focussing with confocal optical detection." Biosensors and Bioelectronics **21**: 1621-1630.

Kennedy, M. J., S. J. Stelick, et al. (2009). "Hydrodynamic focusing with a microlithographic manifold: controlling the vertical position of a focused sample." Microfluidics and Nanofluidics **7**(4): 569-578.

Kim, J. S., G. P. Anderson, et al. (2009). "Multiplexed Detection of Bacteria and Toxins Using a Microflow Cytometer." Analytical Chemistry **81**(13): 5426-5432.

Kummrow, A., J. Theisen, et al. (2009). "Microfluidic structures for flow cytometric analysis of hydrodynamically focussed blood cells fabricated by ultraprecision micromachining." Lab on a Chip **9**(7): 972-981.

Mao, X., S. C. Lin, et al. (2009). "Single-layer planar on-chip flow cytometer using microluidic drifting based three-dimensional (3D) hydrodynamic focusing." Lab on a Chip **9**(11): 1583-1589.

Simonnet, C. and A. Groisman (2006). "High-Throughput and High-Resolution Flow Cytometry in Molded Microfluidic Devices." Analytical Chemistry **78**: 5653-5663.

Tung, Y.-C., M. Zhang, et al. (2004). "PDMS-based opto-fluidic micro flow cytometer with two-color, multi-angle fluorescence detection capability using PIN photodiodes." Sensors and Actuators B: Chemical **98**(2-3): 356-367.

Wang, Z., J. El-Ali, et al. (2004). "Measurements of scattered light on a microchip flow cytometer with integrated polymer based optical elements." Lab on a Chip **4**: 372-377.

Yang, S.-Y., K.-Y. Lien, et al. (2008). "Micro flow cytometry utilizing a magnetic bead-based immunoassay for rapid virus detection." Biosensors and Bioelectronics **24**(4): 855-862.

CHAPTER 3

TRANSVERSE DIFFUSIVE BROADENING IN A MICROFLUIDIC DEVICE WITH THREE-DIMENSIONAL HYDRODYNAMIC FOCUSING

ABSTRACT

A microfluidic diffusion-mixer was experimentally imaged and numerically analyzed that hydrodynamically focuses a solution into the center of a square microfluidic channel using pressure-driven laminar flow. The imaging experiment showed that smaller molecules, represented by fluorescein, diffuse quickly over the cross-sectional area of the microchannel in comparison to larger molecules, represented by Enhanced Green Fluorescent Protein (EGFP). A numerical analysis program was developed that generated simulated concentration distributions for comparison with the experimental images. This program used the moving mesh method in order to simulate the three-dimensional microfluidic channel using a two-dimensional mesh. Using this program, simulated concentration distributions were generated in agreement with the experimental images but which overestimated the diffusion coefficients of fluorescein and EGFP by factors of approximately 1.9±0.4 and 1.4±0.2, respectively. The ultimate source of this over-estimation was hydrodynamic dispersion, which could not be properly accounted for using the moving mesh method. The effect of hydrodynamic dispersion was more pronounced for fluorescein than for EGFP, and the effect was more pronounced at distances downstream, near the outlet of the device, than near the inlet, since the diffusion of the molecules outwards from the center of the microchannel affected their velocity distribution. The present study informs the analysis of solute-transport in microfluidic laminar-flow devices, particularly those for which it is necessary to model the effects of both molecular diffusion and hydrodynamic dispersion.

1. Introduction

Microfluidic focusing devices focus a solution into a subregion of a microfluidic channel. Hydodynamic focusing is achieved by impinging the solution-under-focusing on one or more sides by pressure-driven focusing fluids. A laminar flow-based diffusion-mixer can be developed by embodying a hydrodynamic focusing manifold with a long microfluidic channel where diffusive mixing takes place. Solutes present in the focusing fluids diffuse into the solution-under-focusing and vice versa. By acquiring measurements at distances along the length of the microchannel, proteins can be observed as they fold under changing solution conditions (Kauffmann, Darnton et al. 2001). In addition, laminar flow-based diffusion-mixers have been used to construct novel materials including gelated microfibers (Shin, Park et al. 2007) and self-assembled nanoparticles (Lauchlicht, Cheifetz et al. 2008). Development and use of microfluidic devices for these applications requires a quantitative understanding of solute-transport over the volume of the device.

Two distinct phenomena drive the transport of solutes in a long microfluidic channel: hydrodynamic dispersion and molecular diffusion. Hydrodynamic dispersion occurs due to the change in fluid velocity from zero at the walls of the microchannel to maximum at its center. Molecular diffusion occurs due to the Brownian movement of the solute molecules. These two phenomena act in orthogonal directions: hydrodynamic dispersion and molecular diffusion transport the solutes parallel and transverse[3] to the direction of flow, respectively. For many devices these two effects cannot be decoupled from one other, which presents a challenge for device-modeling and characterization.

---

[3] Molecular diffusion is a three-dimensional phenomenon, however its effect along the direction of flow is typically small in comparison to that of hydrodynamic dispersion and can therefore be ignored.

Three-dimensional (3-D) hydrodynamic focusing devices focus the solution away from all four walls of the microchannel typically into a cylindrical lamina.[4] The present microfluidic device is constructed from two layers and achieves 3-D focusing by impinging the solution from above and below with focusing fluids from the adjoining layer, as shown in Figure 16. By mitigating the effect of the walls, 3-D focusing is thought to reduce the effect of hydrodynamic dispersion on the molecules-under-focusing. Kauffman et al. used a three-dimensional focusing manifold to study the folding of a denatured globular protein (Kauffmann, Darnton et al. 2001), and Lipmen et al. used a similar device with FRET to study the folding kinetics of the heat-shock protein (Lipman, Schuler et al. 2003). However, the diffusive broadening in these devices was not characterized using either experiment or simulation. In fact, the present work is the first examination on the transverse diffusive broadening of a 3-D focused solution.

In the present device, the microchannel is constructed from a large orifice compared with those used previously to study protein folding. Specifically, the diffusion zone in the present device is constructed from a smallest dimension of 125 μm compared with dimensions as small as 8 μm in the previous diffusion-mixers (Kauffmann, Darnton et al. 2001; Lipman, Schuler et al. 2003). Other hydrodynamic focusing devices have been developed by other groups with dimensions equal to or larger than the present device, but these have been intended primarily for flow cytometry (Golden, Kim et al. 2009; Kummrow, Theisen et al. 2009; Mao, Lin et al. 2009), and none of these have been characterized for diffusive broadening. Owing to its large orifice, the present device is suited, ultimately, for kinetics studies on cells rather than on proteins.

---

[4] Strictly speaking, cylindrical focusing acts in only two-dimensions, however in practice the microfluidics community has referred to this as 3-D focusing.

Multiphysics software packages have provided a common platform for the design and modeling of microfluidic devices. These programs can solve both the Navier-Stokes equation and convection-diffusion equation using a 3-D finite element model. In this manner, multiphysics programs are able to account for both hydrodynamic dispersion and molecular diffusion and are able to model transport with high fidelity so long as the flow is kept laminar. However, multiphysics programs begin to fail as the length of the microchannel becomes large compared with its width. For example, Kamholz et al. used multiphysics software to simulate a long microchannel, but using a run-time of 1 day the program required a mesh so course that the solution could not be quantitatively compared with experiment (Kamholz, Shilling et al. 2001). Similar multiphysics simulations were performed by Lipman et al., but again there was no comparison with experiment, and inspection of the figures suggests that again the mesh was too course to provide quantitative diffusion results (Lipman, Schuler et al. 2003). Indeed, to the knowledge of the authors, a multiphysics-based solution to the convective-diffusion equation for a long microfluidic channel has not yet been verified by experiment.

A simple $t^{1/2}$ scaling law has been used to describe transverse diffusive broadening in a microfluidic diffusion mixer (Ismagilov, Stroock et al. 2000). This analytical approach provides a quantitative description of diffusive broadening on length-scales that fall outside the range of multiphysics programs. However, the $t^{1/2}$ scaling law can only be used in the limited case in which the focused distribution is small compared with the enclosing geometry. Unlike the device used previously by Ismagilov et al. (Ismagilov, Stroock et al. 2000), which focused the solution into a thin columnar lamina, the present device focuses the solution into a cylindrical lamina. Importantly, the present study concerns a cylindrical lamina which has not been focused arbitrarily small, but for which the volume of the solution-under-focusing is equal to 1/10 the

total volume of fluid. Since the $t^{1/2}$ scaling law is valid only when the size of the focused distribution is equal to or less than 1/100 the size of the microchannel (see Appendix 1), the $t^{1/2}$ scaling law cannot be applied in the present study.

For situations where multiphysics simulation is not practical, custom-scripted numerical analysis programs have been developed. In this way, programs can be developed which assume approximations that are not straightforward to implement within the framework of commercial multiphysics software. For example, Kamholz et al. developed a finite difference (FD)-based simulation program that assumed the velocity everywhere was equal to the mean fluid velocity (Kamholz, Weigl et al. 1999). This program ignored the effect of hydrodynamic dispersion yet provided, for the first time, simulated concentration distributions of sufficiently high resolution for quantitative comparison with experimental images. Using this program, a simple microfluidic device was characterized for the diffusive broadening of several proteins including human serum albumin, biotin, insulin, ovalbumin, and streptavidin (Kamholz, Weigl et al. 1999; Kamholz, Shilling et al. 2001). To date, this method of simulation has been used only by Kamholz et al. and has yet to be repeated independently by another group. Therefore, additional studies would be useful for corroborating the previous results.

Since the initial studies on the analysis of transverse diffusive broadening (Kamholz, Weigl et al. 1999; Ismagilov, Stroock et al. 2000; Kamholz, Shilling et al. 2001; Kamholz and Yager 2002), new hydrodynamic focusing devices have been developed. In the present work, the analysis of transverse diffusive broadening has been revisited using a new microfluidic device and using improved numerical analysis methods. Following Kamholz et al. (Kamholz, Weigl et al. 1999; Kamholz, Shilling et al. 2001), a FD-based numerical analysis program was developed, and the fluid-velocity was assumed not to vary in the transverse directions. Whereas previous diffusion-mixing

studies used a microfluidic channel of high aspect ratio in order to approximate the microchannel as infinitely wide (Darnton, Bakajin et al. 2001; Kauffmann, Darnton et al. 2001), the present study uses a microchannel of square cross-section. This necessitates the use of a 2-D mesh as opposed to a 1-D mesh for modeling the microfluidic channel using the moving mesh method.

'

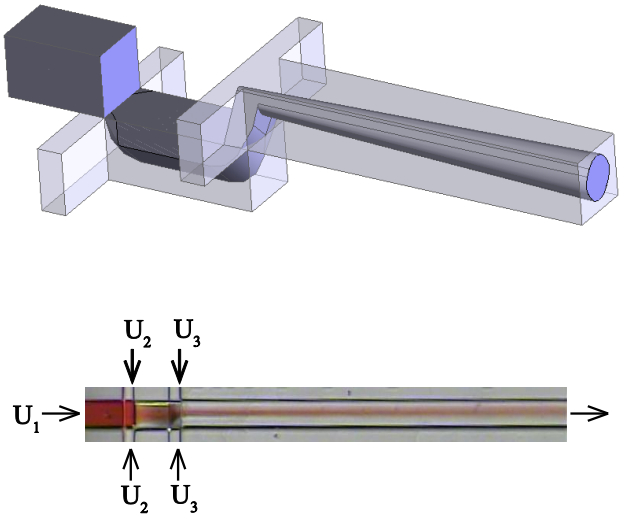

Figure 16. Microfluidic device and operation. (Top) Conceptual rendering shows the hydrodynamic focusing manifold leading to a long microfluidic channel. (Bottom) Brightfield micrograph shows the device with the solution-under-focusing loaded with food coloring. Only a portion of the length of the device is shown due to the limited field of view of the optical microscope. The microfluidic channel was 125 μm wide and 16,000 μm long.

2. Theory and Computation

2.1 FD approximation to the diffusion equation.

A distribution of molecules undergoing the Brownian movement follows the diffusion equation

$$\frac{\partial c}{\partial t} = D\left(\frac{\partial^2}{\partial x^2} + \frac{\partial^2}{\partial y^2}\right)c \tag{1}$$

where D is the coefficient of molecular diffusivity and c represents the concentration of the solutes.

The diffusion equation can be solved numerically using the FD method. Within the fully explicit Forward-Time Centered-Space (FDCS) scheme (Press, Flannery et al. 1986), the time derivative and spatial Laplacian derivative can be approximated by the following two equations, respectively, where i is incremented in the x-direction, j in the y-direction, and k in time.

$$\frac{\partial c}{\partial t} = \frac{c_{i,j}^{k+1} - c_{i,j}^{k}}{\delta t} \tag{2}$$

$$\nabla^2 c = \frac{c_{i,j}^{k} - 2c_{i,j}^{k} + c_{i,j}^{k}}{\delta x^2} + \frac{c_{i,j+1}^{k} - 2c_{i,j}^{k} + c_{i,j-1}^{k}}{\delta y^2} \tag{3}$$

The diffusion equation (Equation 1) can be approximated by combining the two equations above. Using a mesh with square lattice spacing such that $\delta x = \delta y$, the result can be written as follows:

$$c_{i,j}^{k+1} = c_{i,j}^{k} + \delta t \frac{4D}{\delta x^2}\left(\frac{1}{4}c_{i+1,j}^{k} + \frac{1}{4}c_{i-1,j}^{k} + \frac{1}{4}c_{i,j+1}^{k} + \frac{1}{4}c_{i,j-1}^{k} - c_{i,j}^{k}\right) \tag{4}$$

Traditionally, the FD equations have been solved numerically using linear algebra

techniques typically involving matrix inversion (Press, Flannery et al. 1986), which is computationally intensive. In the present work, Equation 4 was solved instead using the FTCS scheme. Notably, the FTCS method is identical to the Generalized Random Walk algorithm, which was recently described in detail for solving the diffusion equation in one dimension (Vamos, Suciu et al. 2003). In the present work, a 2-D FTCS algorithm was developed. This algorithm is best understood by setting the time-step in Equation 4 equal to $\delta t = \delta x^2/4D$, for which case the algorithm, at each time-step, replaces the amount of substance at any given node by the sum of 1/4 the substance from the four nodes immediately above, below, to the right and to the left of itself, as illustrated in **Error! Reference source not found.**.

. Generally, any value of δt may be used so long as $\delta t \leq \delta x^2/4D$, for numerical stability, and the solution is accurate for times large compared with δt (Press, Flannery et al. 1986).

The boundary condition of impermeable walls requires that the spatial derivative of concentration at the location of the wall equal zero in the normal direction. Numerically, this boundary condition has the effect of reflecting outward-directed substance off the wall towards the interior.

The FD-based program for solving the diffusion equation was written as a matlab script. This program was verified by comparing its result for a geometry comprising circular impermeable walls with the known analytical solution to the diffusion equation for a cylindrical pipe (see Appendix 2).

2.2 Velocity field of the carrier fluids.

The fluid-velocity field in a long microfluidic channel under pressure-driven laminar flow is governed by Stokes equation, where $\vec{u}$ represents the velocity field of the fluids and $\vec{\nabla}P$ represents the pressure gradient (Brody, Yager et al. 1996):

$$\vec{\nabla}^2 \vec{u} = \vec{\nabla} P \tag{5}$$

The analytical solution to the Stokes equation has been obtained for a long microchannel of rectangular cross-section and furthermore has been experimentally validated (Lima, Wada et al. 2006). This solution can be written as follows:

$$u_z(x,y) = \sum_{n\ odd} \frac{Q}{n^3}\left(1 - \frac{\cosh(n\pi \frac{y}{h})}{\cosh(n\pi \frac{w}{2h})}\right)\sin(n\pi \frac{z}{h}) \tag{6}$$

where flow is directed in the z-direction and the normalization factor Q is calculated by normalizing the total volumetric flow-rate equal to that applied by the syringe pumps.

2.3 Moving mesh method for solving the convection-diffusion equation.

The convection-diffusion equation couples the molecular diffusion of the solutes to the velocity field of the carrier fluids. The equation is constructed by adding an advective term to the diffusion equation and dropping the time-dependence in order to model the steady-state. For the case that the velocity field points only in the z-direction, the convection-diffusion equation is given as follows:

$$u_z \frac{\partial c}{\partial z} = D\left(\frac{\partial^2}{\partial x^2} + \frac{\partial^2}{\partial y^2}\right)c \tag{7}$$

The first step in solving Equation 7 is to substitute the solution to Stokes equation, *i.e.* Equation 6, into u_z. Generally, the numerical solution requires a 3-D model. However, under the assumption of transverse-uniform fluid velocity, *i.e.*, u_z does not vary with x or y, an approximate solution can be obtained using a 2-D mesh. Commonly referred to as the moving mesh method, a 2-D model is solved repeatedly in discrete steps along the third dimension, as illustrated in Figure 17. The moving mesh method simplifies computation in comparison to a full 3-D model. Using this approach, the convection-diffusion equation for a long microchannel of high aspect ratio has been solved previously using a 1-D mesh (Kamholz, Weigl et al. 1999; Kamholz, Shilling et al. 2001; Kauffmann, Darnton et al. 2001). In the present study, a 2-D mesh is required due to the square cross-section of the microchannel as opposed to a cross-section of high aspect ratio.

Previous moving mesh programs have moved the mesh along the direction of flow at the mean velocity of the fluid medium (Kamholz, Weigl et al. 1999; Kamholz, Shilling et al. 2001; Kamholz and Yager 2002). However, in the present work the mesh was moved at the mean velocity of the molecules-under-focusing, as calculated using the following equation, where $u(x,y)$ was calculated from Equation 6.

$$< u_z > \;=\; \frac{\int\int c(x,y,z)u(x,y)\,dxdy}{\int\int c(x,y,z)\,dxdy} \qquad (8)$$

Moving the mesh at the mean velocity of the solutes rather than that of the carrier fluids prevents the overestimation of the residence time of the molecules (Kamholz, Shilling et al. 2001)

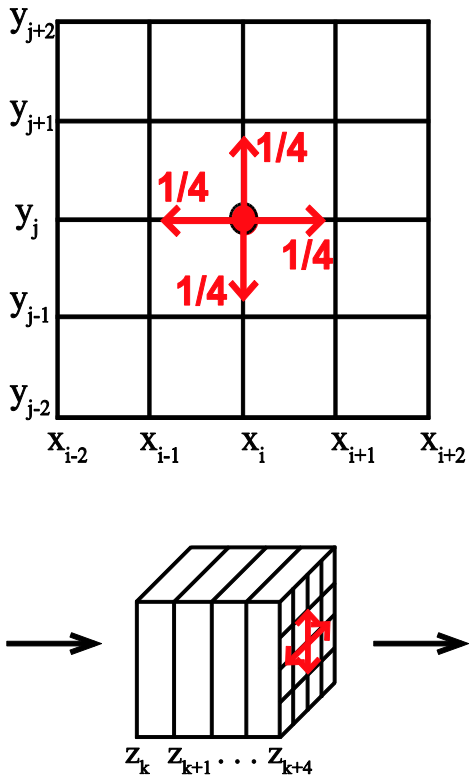

Figure 17. Method of numerical analysis. (Top) Drawing illustrates the 2-D FTCS algorithm on a square lattice. During one time-step δt, one-fourth of the molecules at each node are moved up, down, left, and right to the neighboring node. (Bottom) Drawing illustrates the moving-mesh method. At each step, the mesh is moved along the direction of flow and one iteration of the FTCS algorithm is performed.

2.4 Simulation of the microfluidic device.

Simulation of the device was performed in two stages. In the first stage, the hydrodynamic focusing manifold was simulated using multiphysics software. In the second stage, the long microfluidic channel was simulated using the moving-mesh method. The solution from the first stage of simulation served as the initial condition for the second stage.

The hydrodynamic focusing manifold was solved using ANSYS Multiphysics version 10.0 as in our previous work (Kennedy, Stelick et al. 2009). Briefly, approximately 1 mm length of the device was meshed with a characteristic mesh length of 5 μm. A steady-state solution was obtained by solving, together, the Navier-Stokes equation and the convection-diffusion equation using 100 iterations of the preconjugated residual method solver in ANSYS. The solution was obtained within approximately 1 hour using a personal computer.

In order to feed the multiphysics solution into the moving mesh program, a portion of the multiphysics model, specifically a 10-μm thick cross-sectional slice of the microchannel located a distance of 100 μm downstream from the last junction of the manifold, which included approximately 2,000 nodes, was exported into a textfile using the *nsel* and *nlist* commands in ANSYS. These nodes and their corresponding velocity-values and concentration-values were imported into matlab where they were interpolated onto a flat 2-D mesh using the *griddata* command.

The simulation program used a 2-D grid of 251 x 257 nodes (125 x 128 μm) for a total of 64,507 nodes. Taking 18,000 steps in the direction of flow, the simulation along the entire 1.5 cm of the microfluidic device was accomplished in less than two minutes using a laptop PC with an Intel Core-2 Duo 2.1 GHz processor.

The experimental images contained optical noise. In order to mimic the optical detection process, Gaussian noise was added to the simulated concentration

distributions with a mean-value of zero and a variance of 2.7e-3 or 1.2e-3 for fluorescein or EGFP, respectively, using the *imnoise* function in matlab. Different quantities of noise were necessary because during image acquisition the optical gain of the detection system was adjusted upon switching substances. It was found by inspection of the images and simulations that the levels of computer-generated noise used here matched approximately the noise present in the experimental images. The noise was added to the simulated concentration distributions post-run-time and did not affect the numerical solution.

3. Experimental Methods

3.1 Microfluidic Device and Operation.

The microfluidic device consisted of a microfluidic hydrodynamic focusing manifold and a diffusion mixer. The diffusion mixer comprised a long microchannel at the output of the focusing device and provided the length necessary for diffusion to occur. The dimensions of the diffusion mixer microchannel were 125 μm x 125 μm x 16,000 μm. The focusing manifold comprised two complimentary pieces of polydimethylsiloxane (PDMS) arranged onto one another such that the solution-under-focusing was impinged first from below and then from above by focusing fluids. The fabrication protocol was described in detail in our previous work (Kennedy, Stelick et al. 2009). Briefly, the PDMS pieces were molded from silicon masters, which were fabricated by photolithographic patterning of polyimide resist.

The solution-under-focusing was injected into the primary inlet at rate U_1. Focusing fluids were injected at rate U_2 into the first stage of focusing, which impinged the solution-under-focusing from below, and at rate U_3 into the second stage of focusing, which impinged the solution-under-focusing from above. Each stage of focusing used twin inputs from opposing sides such that the total volumetric flow-rate was equal to

$U_{TOT} = U_1+2U_2+2U_3$. Altogether, the device contained five fluid inputs and required three independently controllable syringe pumps. In the present study, the volume of the solution-under-focusing as a fraction of the total fluid was fixed at $U_1/U_{TOT} = 1/10$. The configuration of flow-rates, U_1, U_2, and U_3, required to focus the solution into the center of the microchannel at each volumetric flow-rate of operation, U_{TOT}, was determined using multiphysics software according to the methods described in detail in our previous work (Kennedy, Stelick et al. 2009).

3.2 EGFP expression and purification.

EGFP was expressed on a pET plasmid in a C41 strain on E. coli. The cells were grown in yeast extract medium and induced in IPTG. The harvest cell density was approximately 70 grams of dry cell weight per liter of broth. The cells were pelleted using centrifugation and resuspended in 20 mM Tris buffer pH 8.0. The resuspended cell pellet was sent through a high pressure homogenizer for three passes at 20,000 psi peak pressure to break open the cells. The insoluble protein and cell debris were then separated from the soluble protein by centrifugation. The EGFP was in the soluble fraction.

3.3 Preparation of the fluorescent solutions.

Fluorescein (free acid, molecular weight = 332) and Rhodamine 6G (molecular weight = 479) were purchased from Sigma-Aldrich. Fluorescein was dissolved at a concentration of 2 mM in 50 mM potassium phosphate buffer pH 7.0. EGFP was used, as purified, in 20 mM Tris HCl pH 8.0. Rhodamine was dissolved at a concentration of 2 mM in the same buffer as the fluorescent molecule under study, either fluorescein or EGFP. All solutions were degassed immediately prior to experiment by placing them under pulsed vacuum for 10 minutes.

3.4 Image acquisition.

Images were acquired using the same inverted laser-scanning confocal microscope that was used in our previous work (Kennedy, Stelick et al. 2009). Alignment marks were included in the photolithographic design of the microdevice for alignment of the microscope to specific distances, precise within 10 μm, along the length of the microchannel.

Images were acquired by applying the solution-under-focusing, containing either fluorescein or EGFP, to the sample inlet, while applying a second solution containing rhodamine to the four focusing inlets. The purpose of the rhodamine, which is spectrally independent from fluorescein, was to image the entire cross-section of the microchannel thereby allowing the images to be cropped along the channel walls. The spectral contribution of rhodamine was removed from each image during image processing.

The raw images were inspected with ImageJ. The width and height of the microchannel were measured to be approximately 125 μm and 128 μm with measurement errors of 2 μm and 4 μm in the horizontal and vertical directions, respectively. The measurement error in the horizontal direction arose because the side walls were not perfectly vertical nor perfectly flat. The measurement error in the vertical direction arose because the optical detection process did not yield crisp boundaries at the top and bottom walls of the microchannel. These cross-sectional dimensions did not change noticeably along the length of the microchannel.

3.5 Image processing.

Image processing was necessary to infer the concentration distributions from the fluorescence micrographs. A matlab script corrected for any spatial variations of

fluorescence intensity due to the optical detection system and subtracted out any spectral contribution of rhodamine. At the conclusion of image processing, the processed images were cropped to a common size equal approximately to the size of the microchannel. Each image comprised 251 x 257 pixels with 8-bit values ranging between 0 and 255. For easy viewing, the images shown here were inverted such that the darker regions represent higher concentration. A more detailed description of the image processing steps is given in Appendix 3.

3.6 Image analysis.

The extent of diffusion was quantified by measuring the root-mean-squared-distance (RMS-distance) of the fluorescent molecules from their center of mass according to the following equation:

$$\sqrt{< x^2 + y^2 >} = \sqrt{\frac{\int\int c(x,y,z)\,((x - x_{CM})^2 + (y - y_{CM})^2)\,dxdy}{\int\int c(x,y,z)\,dxdy}} \qquad (9)$$

where the x_{CM} and y_{CM} represent the horizontal and vertical centers of mass, respectively.

The magnitude of hydrodynamic dispersion was quantified by measuring the coefficient of variation (CV) of the species-weighted velocity distribution, CV_u, as calculated using the following equation:

$$CV_u = \frac{100\%}{< u_z >}\sqrt{\frac{\int\int c(x,y,z)\,(u(x,y) - < u_z >)^2\,dxdy}{\int\int c(x,y,z)\,dxdy}} \qquad (10)$$

where $u(x,y)$ and $<u_z>$ were calculated according to Equation 6 and Equation 8, respectively.

4. Results and Discussion

4.1 Diffusive broadening of fluorescein and EGFP.

Fluorescein and EGFP were each focused into the center of the microchannel. An average fluid velocity of 2.2 cm/s was maintained corresponding to Re = 2.7. Images were acquired at distances along the microchannel, and these are shown in Figure 18. All of these images were acquired on a single day by imaging a single device using a 20X objective. Near the entrance of the microchannel, the distributions for fluorescein and EGFP appeared similar to one another, showing that both were hydrodynamically focused with equal effectiveness. However, downstream the distributions were broadened, and the broadening was significantly more extensive for the lower-molecular weight molecule, fluorescein, than for the higher- molecular weight molecule, EGFP. Notably, the interface between the solution-under-focusing and the focusing solution is sharper for EGFP than for fluorescein at the entrance of the microchannel, *i.e.* z = 0.01 cm. This indicates that some diffusion occurred in the 0.05-cm length of the hydrodynamic focusing manifold upstream of the diffusion-mixer microchannel.

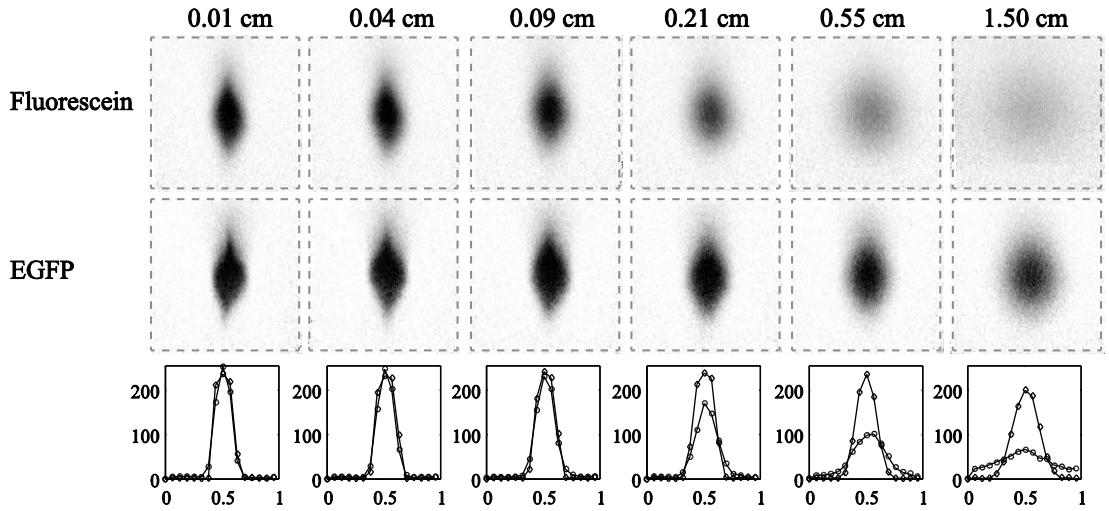

Figure 18. Confocal micrographs show cross-sectional concentration distributions at distances along the microchannel for (Top row) fluorescein and (Middle row) EGFP. (Bottom row) Profiles acquired horizontally across the images show the pixel values representing the concentrations of fluroescein (○) and EGFP (◊). The images consisted of eight-bit integer pixel-values ranging between 0 and 255.

4.2 Simulations and comparison with the experimental images.

Simulated concentration distributions were computed using the moving-mesh method, and these are shown alongside the experimental images in Figure 19. Inspection reveals good agreement between experiment and simulation with regard to overall shape of the concentration distributions. However, there appears a discrepancy between experiment and simulation at distances downstream, nearest to the outlet. Here, at z = 1.5 cm, the fluorescence intensity is brighter in the experimental image than in the simulation. This discrepancy reveals a shortcoming of the moving-mesh method of simulation: mass is not conserved. In nature, the conserved quantity is not the total quantity of mass on a cross-section of the microchannel, $\int c(x,y,z)dxdy$, but the total quantity of mass-flux, $\int c(x,y,z)u_z(x,y)dxdy$. Conserving mass-flux, as dictated by nature, is not possible using the moving mesh method.

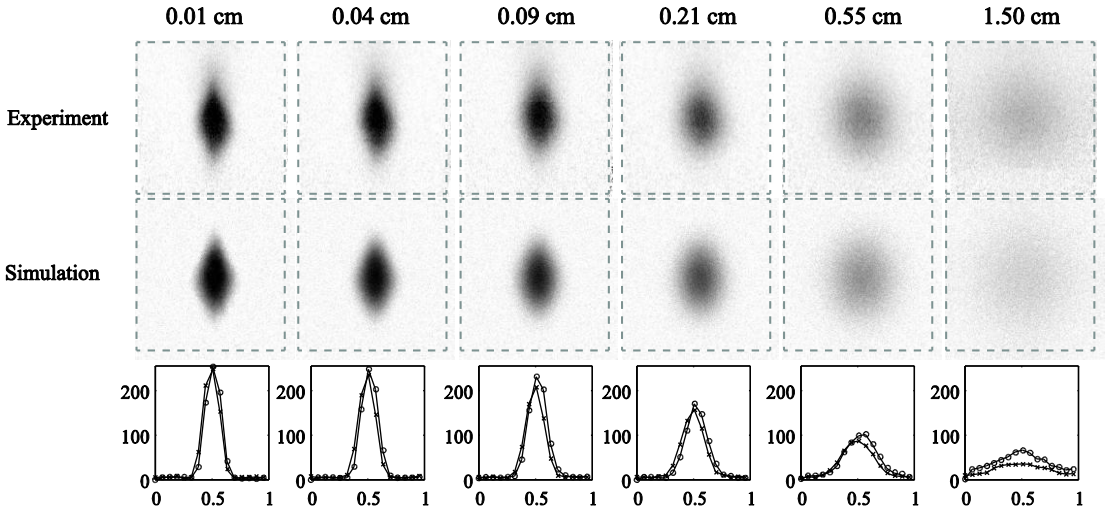

Figure 19. Comparison between simulations and experiment. Top row: Confocal micrographs show the distribution of fluorescein at distances along the microchannel. Middle row: Simulated images. Bottom row: Plots showing profiles acquired horizontally across the experimental images (○) and simulations (x).

4.3 Estimated diffusion coefficients for fluorescein and EGFP.

The experimental images were analyzed yielding the RMS-distance of the molecules from their center-of-mass. Simulations were performed using the moving mesh method, and these were analyzed in the same manner as the experimental images. For both fluorescein and EGFP, the RMS-distance was observed to increase monotonically along the length of the microchannel. These data are plotted along with best-fit simulations, which used diffusion coefficients D_{Fluor} = 1.0±0.1 x 10^{-9} m^2/s and D_{EGFP} = 1.2±0.2 x 10^{-10} m^2/s, in Figure 20. A higher background signal was observed for fluorescein compared with EGFP because, during image acquisition, the photodetecor voltage and laser-transmission percentage were adjusted upon switching substances.

Notably, a second experiment was performed with fluorescein, specifically in which the flow-rate was varied, and this experiment was performed on a different day with a different replica-device. The second experiment yielded a best-fit diffusion coefficient of D_{Fluor} = 9.0 x 10^{-10} m^2/s, as reported in Appendix 4. Therefore, the best-fit diffusion coefficient varied by 10% between two experiments, which provides an indicator of the precision of the current measurement technique. By taking the average of these two measurements, the moving mesh method resulted in an estimated diffusion coefficient for fluorescein equal to 9.5±0.7 x 10^{-10} m^2/s.

The diffusion coefficient of fluorescein has been measured previously by longitudinal broadening of plugs in microchannels and by observation of diffusion from polymers into unstirred fluids as D_{Fluor} = 4.25 x 10^{-10} m^2/s in water (Culbertson, Jacobsen et al. 2002) and D_{Fluor} = 5.5 x 10^{-10} m^2/s in PBS (Radomsky, Whaley et al. 1990), respectively. If, by averaging these two measurements, the true diffusion coefficient is assumed to equal D_{Fluor} = 4.9±0.9 x 10^{-10} m^2/s for fluorescein in the present buffer, 50 mM potassium phosphate pH 7.0, then the best-fit simulations overestimated the diffusion coefficient of fluorescein by a factor of 1.9±0.4.

The diffusion coefficient of EGFP should be similar to that of native green fluorescent protein (GFP), which has been measured previously. The diffusion coefficient of native GFP has been measured previously as D_{GFP} = 8.7 x 10^{-11} m^2/s using the photobleaching recovery technique (Swaminathan, Hoang et al. 1997) and D_{GFP} = 8.3 x 10^{-11} m^2/s using the fluorescence correlation microscopy technique (Guiot, Enescu et al. 2000). The true diffusion coefficient of EGFP was assumed to equal the average of these two measurements, that is D_{EGFP} = 8.5±0.3 x 10^{-11} m^2/s. The experimental data in the present work was best fit by D_{EGFP} = 1.2±0.2 x 10^{-10} m^2/s. Therefore, the present simulation program overestimated the diffusion coefficient of EGFP by a factor of 1.4±0.2.

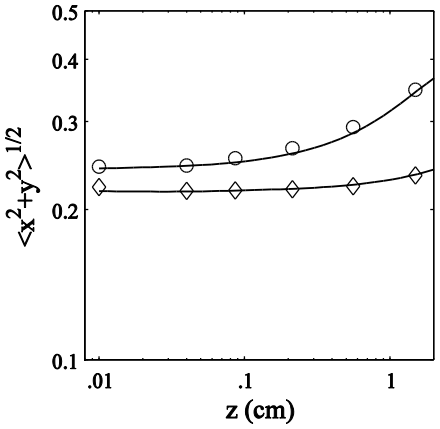

Figure 20. Plot shows the RMS-distance of distributions of fluorescein (○) and EGFP (◊) molecules from their centers-of-mass at distances along the microchannel. The best-fit simulations, shown here, used diffusion coefficients D_{Fluor} = 1.0 x 10^{-9} m^2/s and D_{EGFP} = 1.2 x 10^{-10} m^2/s.

4.4 Hydrodynamic dispersion of fluorescein and EGFP.

The velocity distribution of the molecules can be obtained using knowledge of the concentration distribution combined with the velocity field known for a long rectangular pipe. Histograms show the velocity distributions of Fluorescein and EGFP in Figure 21. At distances downstream the velocity distribution was much broader for fluorescein than for EGFP. These histograms were constructed using the best-fit simulations shown previously in Figure 20. The diffusion outwards of the molecules-under-focusing effected the broadness of their velocity-distribution and also their mean velocity. The slowing of the molecules was significantly more pronounced for fluorescein than for EGFP. Specifically, the mean velocity of the fluorescein molecules slowed by 31% along the length of the microchannel whereas that of EGFP slowed by only 5%. In addition, the CV of the velocity-distribution, which provides a direct gauge of the magnitude of hydrodynamic dispersion, increased by a factor of seven along the length of the microchannel for fluorescein and by a factor of only two for EGFP, as shown in Figure 22.

. The present device significantly reduced the magnitude of hydrodynamic dispersion for EGFP, for which the CV of its velocity-distribution approached only 10% even near the outlet of the microchannel. For comparison, the CV of the velocity distribution is 63% for a uniformly distributed solution traveling through a square pipe.

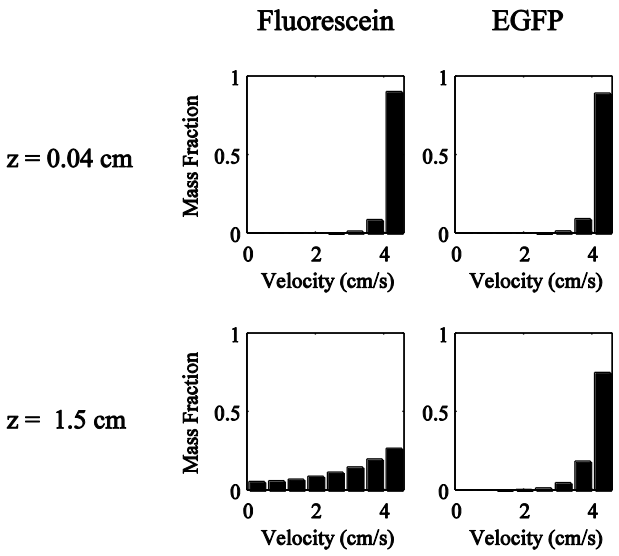

Figure 21. Histograms show the species-weighted velocity distributions for fluorescein and EGFP near the entrance of the microchannel (Top row) and near the outlet (Bottom row).

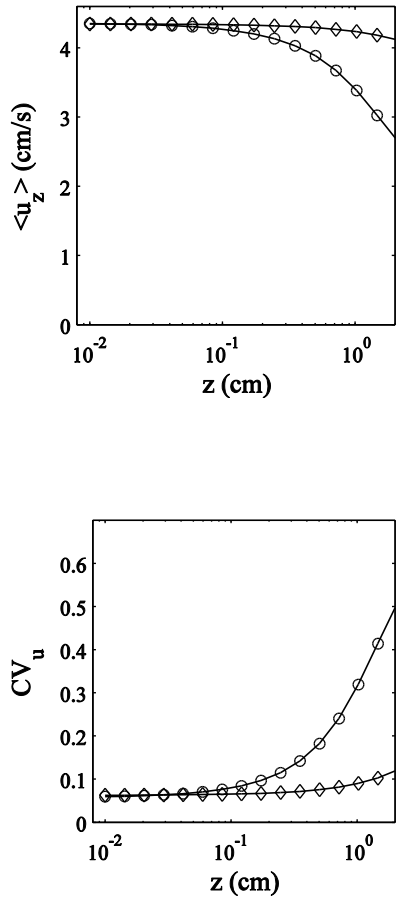

Figure 22. Velocity distribution of the focused molecules. (Top) Plot shows the mean velocity of the focused molecules along the length of the microchannel. (Bottom) Plot shows the CV of the velocity-distribution of the focused molecules along the length of the microchannel. Fluorescein = ○, and EGFP = ◊. The limiting case of a uniform distribution of molecules, which occurs at $z = \infty$, corresponds to mean velocity $\langle u_z \rangle_{z=\infty}$=2.2 cm/s, and $CV_{u,\, z=\infty}$ = 63%.

5. Conclusions

A microfluidic diffusion-mixer was experimentally imaged and numerically analyzed. Owing to its large orifice, the mixer is suited for the analysis of cells analogous to previous studies on the folding-kinetics of proteins. Other potential applications include the synthesis and assembly of novel materials including microfibers, liposomes, and nanoparticles.

A numerical analysis program was developed following generally the approach of Kamholz et al. (Kamholz, Weigl et al. 1999; Kamholz, Shilling et al. 2001; Kamholz and Yager 2002), approximating the fluid-velocity as transverse-uniform in order to solve the 3-D microchannel using a mesh of less than three dimensions. As a consequence of this approximation, the program did not conserve mass, and on comparison with experiment the program over-estimated the diffusion coefficients of fluorescein and EGFP by factors of 1.9±0.4 and 1.4±0.2, respectively. This overestimation was not entirely unexpected, since the seminal study by Kamholz et al. over-estimated the diffusion coefficient of human serum albumin by a factor of two (Kamholz, Weigl et al. 1999). The dominant source of the over-estimation of the diffusion coefficients was hydrodynamic dispersion. Specifically, the program used a moving 2-D mesh and did not track the high- or low- velocity molecules as they were pushed beyond or fell behind the mesh. In spite of its inadequacies, the program succeeded in generating simulated concentration distributions with high spatial resolution and in good agreement with the experimental images. In addition, the program was fast. Specifically, using a 2-D mesh containing 251x257 nodes, the program simulated a microchannel using the same run-time, 2 minutes, as a previous program which used only a 1-D mesh with 1x237 nodes (Kamholz, Weigl et al. 1999). In future work, a 3-D numerical analysis program should be developed in order to

quantitatively infer the effect of hydrodynamic dispersion on the perceived diffusion coefficient.

Hydrodynamic dispersion exerted a significant effect on the transport of the molecules despite the three-dimensional focusing of the molecules into the center of the microchannel. The effect was augmented by the diffusion of the molecules-under-focusing outwards from the faster-moving fluids into the slower-moving fluids and, therefore, was increasingly pronounced downstream. Additional progress is needed on the numerical analysis of solute-transport in microfluidic devices in order to quantify the effect of hydrodynamic dispersion on molecular diffusion.

Acknowledgement

This work was supported in part by the Ludwig Institute for Cancer Research. Fabrication of the device was performed at the Cornell NanoScale Facility, a member of the National Nanotechnology Infrastructure Network (NNIN), which is supported by the National Science Foundation. Images were acquired at the Microscopy and Imaging Facility of the Cornell University Life Sciences Core Laboratories Center. M.J.K. thanks Sasha L. Perkins for her preliminary work performed during the NNIN Research Experience for Undergraduates (REU) program. M.J.K. thanks Rishard H. Chen for expressing and extracting the EGFP.

Appendixes available

Several appendixes are included providing useful details outside the scope of the central theme of this paper. In the first appendix, it is shown that the $t^{1/2}$ scaling law can be used only when the focused distribution is small compared with the dimensions of the microchannel. In the second appendix, evidence is presented that the FD-based program used in this work accurately solves the diffusion equation for a 2-D geometry

with impermeable walls. In the third appendix, the method of image processing is explained in detail. In the fourth appendix, an additional experiment is reported showing the effect of varying the flow-rate on the diffusive broadening of fluorescein. In the fifth appendix, a matlab script is presented for the FD-based program described in this work and for comparing its result with the analytical solution to the diffusion equation.

APPENDIX 1

Appendix 1: Limitation of the $t^{1/2}$ diffusive scaling law to small distributions

The $t^{1/2}$ scaling law was used by Ismagilov et al. to characterize diffusive broadening in a microfluidic device that focused a solution into a thin columnar lamina (Ismagilov, Stroock et al. 2000). The present device focuses the solution into a cylindrical lamina, but in the present study this lamina was not made arbitrarily small. Specifically, in the present study the solution was focused cylindrically into the central 1/10 area of the microchannel.

It was not known at the beginning of this study whether the $t^{1/2}$ scaling law could be used to model the diffusive broadening due to the relatively large size of the focused distribution relative to the size of the microchannel. Therefore, the effect of the tightness of hydrodynamic focusing on the time-scale of diffusive broadening was investigated by placing fictitious initial distributions uniformly distributed within a circular subregion of radius r_0 at the center of a square enclosure with impermeable walls. The size of the initial distribution was varied between $r_0/a = 0.01$ and $r_0/a = 0.30$, where a was the length of the enclosing square, and the concentration distribution was obtained as a function of time using the FD program described in the main text. The extent of diffusion was measured for these fictitious distributions by calculating their RMS-distance from their centers-of-mass. Plots of RMS-distance versus time are plotted in Figure 23. Inspection of the plots reveals that the time-scale of broadening approached the $t^{1/2}$ power law asymptotically as the size of the initial distribution decreased. For the purposes of this study, the distributions were found to broaden according to the $t^{1/2}$ power law only when the size of the initial distribution was small compared with the cross-section of the microchannel, specifically when r_0/a

≤ 0.01. In the present study, solutions were focused into the central 1/10 area of the microchannel, corresponding to $r_0 / a \approx 0.18$. Therefore, due to the large size of the focused distribution the $t^{1/2}$ scaling law cannot be used in the present study.

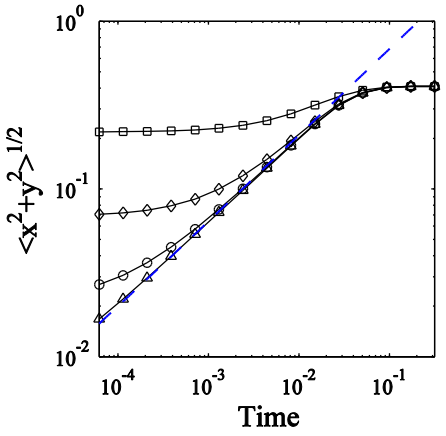

Figure 23. Plot shows the RMS-distance of distributions of molecules from their center-of-mass verses time for initial distributions of radius r_0 = 0.31 (□), r_0 = 0.10 (◊), r_0 = 0.03 (○), and r_0 = 0.01 (△), placed at the center of a square enclosure with impermeable walls. Also plotted is the $t^{1/2}$ scaling law (--), which fits the data only for the smallest initial distribution. All distance measurements are in units of a, the length of each side of the enclosing square, and time is in units of a^2/D.

APPENDIX 2

Appendix 2: Verification of the finite difference-based numerical analysis program for solving the diffusion equation

A finite difference (FD) numerical analysis program was developed to solve the diffusion equation according to the Forward-Time Centered-Difference (FTCS) scheme, as explained in the main text. In order to verify this program, its result was compared with the analytical solution to the diffusion equation for a circular geometry with impermeable walls. An initial distribution of molecules was placed uniformly into the central 1/10 area of a bounding circle. The matlab script for obtaining these two solutions is given in a separate appendix.

Analytical solution to the diffusion equation. For a circular geometry with impermeable walls, the analytical solution to the diffusion equation is given by a sum of Bessel functions (Crank 1975):

$$c(r,t) = 2\int_0^1 r c_0(r)dr + \sum_{n=1}^{\infty} A_n J_0(\lambda_n r) e^{-\pi^2 \lambda_n^2 t} \qquad (1)$$

where the values λ_n are obtained from $J_1(\lambda_n) = 0$ and the coefficients A_n are obtained from

$$A_n = 2 / J_0^2(\lambda_n) \int_0^1 J_0(\lambda_n r)\, r\, c_0(r)\, dr\,,$$

and $c_0(r)$ is the concentration distribution at $t = 0$. In Equation 1, the position variable r has been non-dimensionalized by the pipe radius R, and the time variable t has been non-dimensionalized by the area of the circular enclosure, $\pi R^2/D$. The

nondimensionalization used here differs slightly from Crank's, in which the time variable was non-dimensionalized instead by R^2/D. The present nondimensionalization generates a previously unencountered factor of π in time decay component. The nondimensionalization used presently is superior to that used by Crank because it leads to identical diffusive time-scales for square and circular enclosures provided the area of the enclosure is kept constant.

The concentration distributions determined using Equation 1 were computed in matlab using Bessel function subroutines jyndd and jynzo (Zhang and Jin 1996), which are available for download at http://ceta.mit.edu/ceta/comp_spec_func/. The concentration distribution at any time t was computed to 20 terms in J_0 on a 1-D mesh consisting of 100 equally spaced nodes in less than one minute of run-time using a personal computer.

Main result. A concentration distribution initially distributed uniformly in the central 1/10 area of a circular enclosure is plotted at several times in Figure 24 according to the analytical solution to the diffusion equation and also according to the FD-based numerical analysis program. For the purposes of this work, the two solutions were indistinguishable from one another, as seen in Figure 24. Therefore, it can be concluded that the FD-based computation program used in the present work accurately solves the diffusion equation for a 2-D geometry with impermeable walls for times large compared with δt.

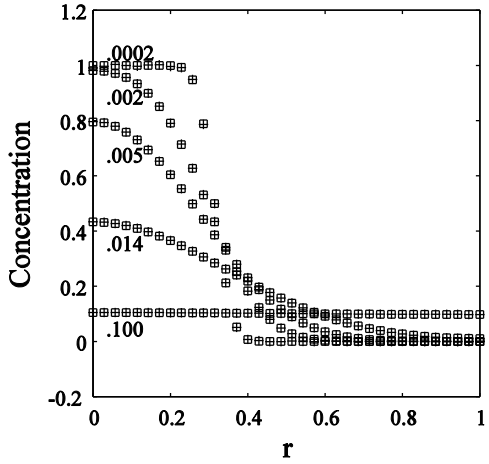

Figure 24. Verification of the FD-based numerical analysis program. Plot shows the concentration versus radial distance for molecules initially distributed uniformly in the central 1/10 area of a circular enclosure with impermeable walls. Times are indicated in units of $\pi R^2/D$, where R is the radius of the bounding circle. Solutions are shown according to the analytical solution to the diffusion equation (+) and according to the FD-based numerical analysis program (□).

APPENDIX 3

Appendix 3: Method of image processing

During image acquisition, two a dark-field image and flat-field images were acquired in addition to the experiental images. The two flat-field images were acquired by applying either the solution-under-focusing, which contained fluorescein or EGFP, or the focusing solution, which contained rhodamine, uniformly to all of the inputs of the device.

For image processing, the experimental image, the two flat-field images, and the dark-field image were all aligned to one another and then processed, using a matlab script, according to the following formula:

$$I(G) = \frac{I(G) - \frac{FF_{Rhod}(G)}{FF_{Rhod}(R)} I(R)}{FF_{Fluor}(G)}$$

where $I(G)$ and $I(R)$ refer to the green and red pixel-values of the experimental image, $FF_{Rhod}(G)$ and $FF_{Rhod}(R)$ refer to the green and red pixel-values of the flat-field image in which rhodamine was applied uniformly to all of the inlets, and $FF_{Fluor}(G)$ refers to the green pixel-values of the flat-field image in which fluorescein was applied uniformly to all of the inlets. Two distinct image-correction steps compose the equation above: the second term in the numerator corrects for the spectral bleedthrough of rhodamine into the green photodetector, and the denominator corrects for the spatial variation of fluorescence intensity over the cross-section of the microchannel. Importantly, the dark-field image, *DF*, was subtracted from all of the

images prior to their use in the equation above. The various images used in image processing are shown in Figure 25. Here, the original image is brighter near the top wall and dimmer near the bottom wall, and additional variation is present in the horizontal directions. However, these spatial variations in fluorescence intensity are not present in the processed image. The images shown in the main text correspond to the green component of the processed image. In addition, the images shown in the main text were inverted for black-on-white viewing and printing.

Notably, the present method of image processing method differs from our previous work (Kennedy, Stelick et al. 2009). Previously, the quantity of interest was the vertical center of mass of the focused distribution, for which horizontal information was not critical. Therefore, mathematical correction was used to correct for vertical variation in image brightness, and this method of correction did not require the acquisition of the *FF* and *DF* images, saving time. In the present work, however, the quantity of interest required both vertical and horizontal information. Therefore, the method of image arithmetic was used, and *FF* and *DF* images were acquired as needed.

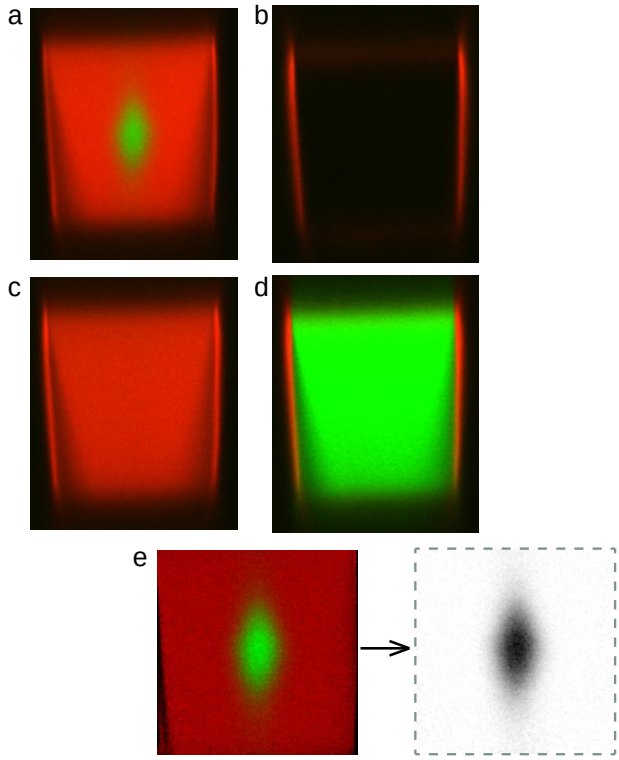

Figure 25. Method of image processing. a Raw experimental image; b Dark-field image; c Flat-field image, rhodamine; d Flat-field image, fluorescein; e Processed image. The main text showed only the green component of the processed image and showed this inverted, in monochrome, for better black-and-white viewing.

APPENDIX 4

Appendix 4: Diffusive Broadening of Fluorescein at different flow-rates

In order to observe the diffusive broadening at different fluid velocities, it was first necessary to find the configuration of relative focusing flow-rates, U_2 and U_3, which positioned the solution-under-focusing at the center of the microfluidic channel. Importantly, as the total volumetric flow-rate, U_{TOT}, was increased, the hydrodynamics were affected such that different focusing ratios, U_3/U_2, were needed. The focusing ratio, U_3/U_2, that positioned the solution-under-focusing at the center of the microfluidic channel was obtained for each of three fluid velocities, corresponding to Reynolds numbers Re = 1.0, Re = 2.7, and Re = 7.4 (see Table 3), prior to experiment by simulating the hydrodynamic focusing manifold using ANSYS Multiphysics version 10.0 according to the methods described in our previous work (Kennedy, Stelick et al. 2009).

An experiment was performed similar to that described in the main text. Fluorescein was focused into the center of the microchannel, and the device was operated at three volumetric flow-rates listed in Table 3. Images were acquired at distances along the microchannel, and these are shown in Figure 26. All of these images were acquired on a single day by imaging a single device with a 10X objective. The images acquired at the three flow-rates appeared similar to one another nearest to the entrance of the microchannel, at z = 0.01 cm, where all three images show the fluorescein focused into a region occupying the central 1/10 area of the cross-section of the microchannel. Downstream, the extent of diffusion was greater at slower rates of flow, as expected.

Logarithmic steps were used to determine the distances along the microchannel at which images were acquired and also the flow-rates at which the device was operated.

Consequently, the images in Figure 26 appear similar to one another when downwards-right diagonally. It follows that a desired distribution of molecules can be obtained by either adjusting the flow-rate or by moving along the length of the microchannel. That is, the extent of diffusion can be tuned hydrodynamically by adjusting the volumetric flow-rate.

The images were analyzed yielding the RMS-distance of the fluorescein molecules from their center-of-mass, and this quantity was observed to increase monotonically along the length of the microchannel, with a greater increase observed at lower flow-rates (Figure 27). Notably, the RMS-distance was abnormally high for the data-point nearest the entrance of the microcahnnel, at z = 100 μm, and upon detailed inspection of the raw images, this was found to result from a high quantity of optical noise due to reflections off the nearby microfluidic junction. This abnormality was not observed in the experiment presented in the main text. The device used for the experiment presented in this appendix was constructed from a thicker device-molding, which necessitated a switch from a 20X objective lens, which was used for the experiment described in the main text, to a 10X objective lens. It is believed that the lower-NA objective collected additional reflections off the walls of the microfluidic junction nearest the inlet. Consequently, the images nearest the inlet contained an abnormally large quantity of optical noise.

The data in Figure 27 were best-fit using the moving mesh program using a diffusion coefficient of $D_{\text{Fluor}} = 9.0 \times 10^{-10}$ m^2/s. A common diffusion coefficient was used to fit the three sets of data acquired at three rates of flow, which supports the conclusion that the extent of diffusion can be tuned either by moving the point of observation along the direction of flow or by adjusting the flow-rate.

The data-sets presented in this appendix and in the main text were best fit using diffusion coefficients, D_{Fluor}, that varied by a factor of 10%, between the two

experiments. This variation most likely resulted from the use of two different objectives and two different photodetector gains between the two experiments. In future work, these devices should be fabricated in such a way that the device-molding thickness remains constant from device-to-device, allowing for the use of a common objective lens between experiments. In addition, in future work it may be preferable to fix the position of the microscope near the end of the microchannel and simply sweep the fluid velocity. While the hydrodynamics would affect the location of the distribution, the optical noise would remain constant from image to image and, furthermore, the images would be easier to align and compare with one another.

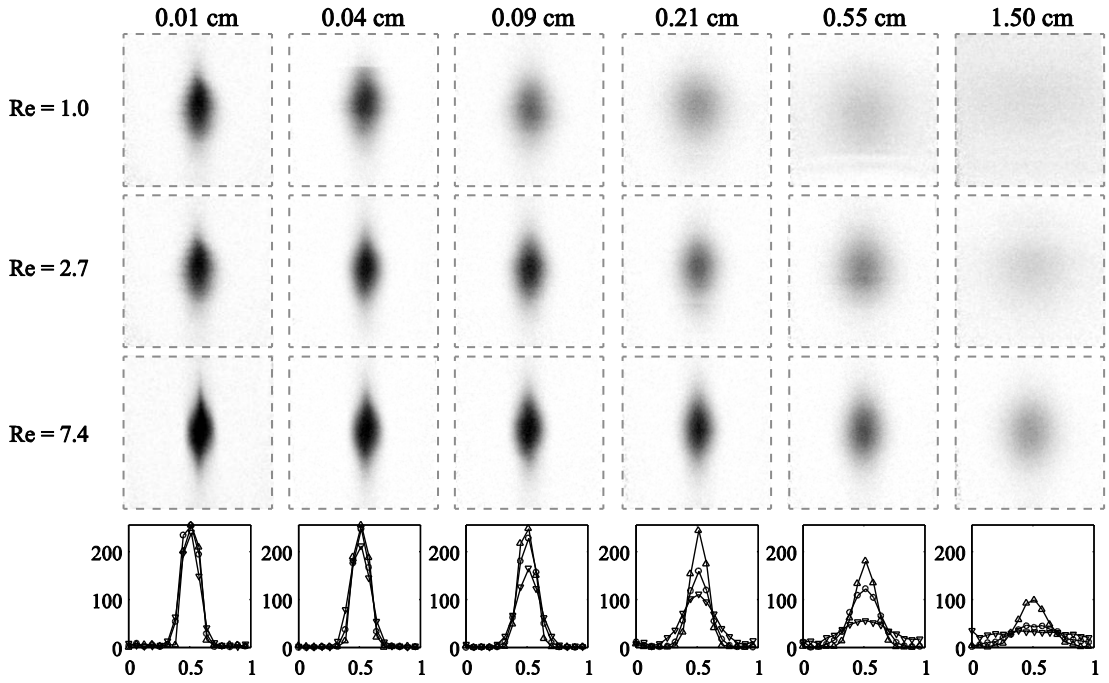

Figure 26. Confocal micrographs show the distribution of fluorescein at six distances along the microchannel for operation at *Re* = 1.0 (Top row), *Re* = 2.7 (Second Row), *Re* = 7.4 (Third row). Profiles acquired horizontally across the images show pixel-values representing concentration for *Re* = 1.0 (▼), *Re* = 2.7 (○), *Re* = 7.4 (Δ) (Bottom row).

Table 3. Flow-rates of operation of the microfluidic device[5].

Re	u_{AVG}	U_3/U_2	U_1	U_2	U_3
1.0	0.8 cm/s	1.57	0.8 µL/min	1.3 µL/min	2.1 µL/min
2.7	2.2 cm/s	1.73	2.0 µL/min	3.4 µL/min	5.8 µL/min
7.4	5.9 cm/s	1.92	5.5 µL/min	8.5 µL/min	16 µL/min

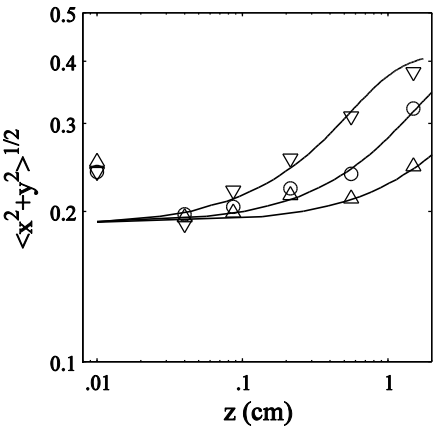

Figure 27. Plot shows the RMS-Distance of distributions of fluorescein molecules from their center-of-mass at distances along the microchannel for three different flow-rates: *Re* = 1.0 (▼), *Re* = 2.7 (○), *Re* = 7.4 (Δ). The best-fit simulation, shown here, was obtained using $D_{\text{Fluor}} = 9 \times 10^{-10}$ m^2/s.

[5] Focusing the molecules into the center of the channel at different Reynolds numbers was achieved by adjusting the ratio between the flow-rates of the top and bottom focusing fluids, U_3/U_2. The fraction of fluid under focusing relative to total fluid was fixed at $U_1/U_{\text{TOT}} = 1/10$.

APPENDIX 5

Appendix 5: matlab script for the finite difference-based numerical analysis of diffusion in two dimensions

MATLAB CODE

```
%-----------------------------------------------------------------
% FTCS-2D.m
%
% The FD solution to the diffusion equation is obtained using
% the Forward-Time Centered-Space (FTCS) method for an initial
% distribution enclosed by circular impermeable walls.
%
% The FTCS solution is compared with the analytical solution
% of the diffusion equation in cylindrical coordinates.
%
% Updated January 29, 2010
% Matthew Kennedy
%-----------------------------------------------------------------
clear all

Radius=100;    % Radius = 100 um
dx = 1*10^-6;  % dx = 1 um

R = (Radius / dx)*10^-6;  % Radius in units of dx
```

```
NX = 2*round(R)+2;   % Number of pixels of mesh, x direction
NY = 2*round(R)+2;   % Number of pixels of mesh, y direction

D = 4.5*10^-10;     % Diffusion coeficient (m2/s)
dt = dx*dx/(4*D);   % time step between iterations of the GRW algorithm
DIFFTIME = pi*R^2*dx^2/D;   % Diffusion time based on area of circle

% Look at distributions at the following fractions of the diffusion time
EVENTLIST = round( [.0002 .002 .005 .014 .1]*DIFFTIME/dt );

cInitial = zeros(NY,NX);
cSave = zeros(NY,NX, size(EVENTLIST,2));
c = zeros(NY, NX);

XC = NX/2;
YC = NY/2;
for l = 1:NY
   for m = 1:NX
      if( ((m-XC)^2+(l-YC)^2)^.5 < R*sqrt(1/10) )
         cInitial(l,m) = 1;
      end
   end
end
c = cInitial;

%---------------------------------------------
```

```
% Define the impermeable boundaries of the geometry
%
WB = zeros(NY,NX); %Within Boundary
LB = zeros(NY,NX); %Left Boundary
RB = zeros(NY,NX); %Right Boundary
BB = zeros(NY,NX); %Bottom Boundary
TB = zeros(NY,NX); %Top Boundary
for i = 1:NX
   for j=1:NY
      if( sqrt( (XC-i)^2+(YC-j)^2 )/R <= 1 && sqrt( (XC-i-1)^2+(YC-j)^2)/R > 1)
         LB(j,i) = 1;
      end
      if( sqrt( (XC-i)^2+(YC-j)^2 )/R <= 1 && sqrt( (XC-i+1)^2+(YC-j)^2)/R > 1)
         RB(j,i) = 1;
      end
      if( sqrt( (XC-i)^2+(YC-j)^2 )/R <= 1 && sqrt( (XC-i)^2+(YC-j-1)^2)/R > 1)
         TB(j,i) = 1;
      end
      if( sqrt( (XC-i)^2+(YC-j)^2 )/R <= 1 && sqrt( (XC-i)^2+(YC-j+1)^2)/R > 1)
         BB(j,i) = 1;
      end
      if( sqrt( (XC-i)^2+(YC-j)^2 )/R <= 1)
         WB(j,i) = 1;
      end

   end
```

```
end

% "crf" = concentration received from above, left, etc.
crfAbove = zeros(NY, NX); crfBelow = zeros(NY, NX);
crfLeft = zeros(NY, NX); crfRight = zeros(NY, NX);
crfNoMove = zeros(NY, NX);
% Amount which does not move due to reflection off wall
NoMoveMatrix = zeros(NY, NX);
NoMoveMatrix = 1/4*(LB+RB+TB+BB);

%------------------------------------------------------------
% Perform the GRW Algorithm
%
saveEvent=1;
cOld = c;
for i = 1:max(EVENTLIST)
   % Amount received from the node above, from below, from left and from
   % right
   crfAbove(2:NY,:) = 0.25*cOld(1:NY-1,:);
   crfBelow(1:NY-1,:) = 0.25*cOld(2:NY,:);
   crfLeft(:,2:NX) = 0.25*cOld(:,1:NX-1);
   crfRight(:,1:NX-1) = 0.25*cOld(:,2:NX);
   % Amount at each node which did not move
   crfNoMove = cOld.*NoMoveMatrix;

   c                                    =                                    cOld*(1-
```

```
4*D*dt/dx^2)+(4*D*dt/dx^2)*(crfAbove+crfBelow+crfLeft+crfRight).*WB+(4*D*dt
/dx^2)*crfNoMove;
   cOld = c;

   % Save distribution at select times for output to screen
   if(i == EVENTLIST(saveEvent))
      cSave(:,:,saveEvent) = c;
      saveEvent = saveEvent+1;
   end

end

%-----------------------------------------------------------------
% Bessels Solution
% Matthew Kennedy
% 29 Dec 2007
%
% Dye Concentration C=1 between r=a1,a2 within cylinder of radius R=1
% Given this initial situation at t=0, find concentration distribution
% at time t.
%
NumTerms=20;             % Compute out to J_NumTerms
Resolution=201;          % Spatial Resolution over r [0,1]
a1=0;a2=sqrt(1/10);      % concentration(r,t=0) = 1 on r in [a1,a2]
t = EVENTLIST*dt/DIFFTIME;
TimeSteps=size(t,2);
```

```
r=0:1/(Resolution-1):1;
r1 = 0:-0.5/(Resolution-1):-0.5;
r2 = 0:0.5/(Resolution-1):0.5;

A=zeros(TimeSteps,Resolution);
A0=2*ones(TimeSteps,Resolution)*quad(@(x) x,a1,a2); % compute A_0
A=A0;   % t=infinity component of the solution

[n,nt,lamda]=jyzo(1,NumTerms);%compute NumTerms zeros of J1

CN = zeros(1,Resolution);
for k=1:TimeSteps
   for n=1:NumTerms     % compute coefficients A_n and add while computing
   [a b BN] = jyndd(0,lamda(n));
   A(k,:)=A(k,:)+2/BN^2*AInteg(lamda(n),a1,a2)*exp(-
lamda(n)^2*pi*t(k))*besselfunctionCSF(0,lamda(n)*r);
   end
end

%---------------------------------------------------------------
% Plot Profiles of Concentration vs. time
figure; hold on
set(0, 'DefaultAxesFontName', 'Times New Roman');
set(0, 'DefaultTextFontName', 'Times New Roman');
set(gcf, 'PaperUnits', 'inches','PaperSize', [3.25 3.25],'Resize','off');
```

```
set(gcf, 'Units','inches');
set(gcf,'Position',[3.25,3.25,3.25,3.25]);

Marker = {' ' ' '};
Marker{1} = 'ks';
Marker{2} = 'ro';

plotXhalf = 0:2/(NX-2):1;
xPlot = 0:1/40:1;
rPlot = 0:1/40:1;

hold on
for i = 1:size(EVENTLIST,2)
   plot(xPlot,interp1(plotXhalf,cSave(round(NY/2),round(NX/2):NX-
1,i),xPlot,'spline'),Marker{1},'MarkerSize',4);
   plot(rPlot,interp1(r,A(i,:),rPlot,'spline'),Marker{2},'MarkerSize',4);
end
ylabel('Concentration','FontName','Times New Roman','FontSize',9);
xlabel('r','FontName','Times New Roman','FontSize',9);
set(gca,'FontSize',7,'FontName','Times New Roman');  % Set tick-label fontsize
axis square
box on;
legend('FD Approx','Analytical Sol.',1);
legend('boxoff');

%
```

```
%---------------------------------------
% besselfunctionCSF.m
%
% Performs repeated calls to the function jyndd on the
%  elements of an array and returns the bessel function of
%  of the input as an array.
%
% jyndd computes the besselfunction Jn(x)
% jyndd was downloaded from http://ceta.mit.edu/ceta/comp_spec_func/
%
function [jOUT] = besselfunctionCSF(Order,x)
jOUT = zeros(1,size(x,2));
for i = 1:size(x,2)
   [a b jOUT(i)] = jyndd(Order,x(i));
end
return
```

REFERENCE

Brody, J. P., P. Yager, et al. (1996). "Biotechnology at Low Reynolds Numbers." Biophysical Journal **71**: 3430-3441.

Crank, J. (1975). Mathematics of Diffusion. Clarendon, Oxford University Press.

Culbertson, C. T., S. C. Jacobsen, et al. (2002). "Diffusion coefficient measurements in microfluidic devices." Talanta **76**(2): 365-373.

Darnton, N., O. Bakajin, et al. (2001). "Hydrodynamics in 2 1/2 dimensions: making jets in a plane." Journal of Physics: Condensed Matter **13**: 4891-4902.

Golden, J. P., J. S. Kim, et al. (2009). "Multi-wavelength microflow cytometer using groove-generated sheath flow." Lab on a Chip **9**(13): 1942-1950.

Guiot, E., M. Enescu, et al. (2000). "Molecular Dynamics of Biological Probes by Fluorescence Correlation Microscopy with Two-Photon Excitation." Journal of Fluorescence **10**(4): 413-419.

Ismagilov, R. F., A. D. Stroock, et al. (2000). "Experimental and theoretical scaling laws for transverse diffusive broadening in two-phase laminar flows in microchannels." Applied Physics Letters **76**(17): 2376.

Kamholz, A. E., E. A. Shilling, et al. (2001). "Optical Measurement of Transverse Molecular Diffusion in a Microchannel." Biophysical Journal **80** (4): 1967-1972.

Kamholz, A. E., B. H. Weigl, et al. (1999). "Quantitative Analysis of Molecular Interaction in a Microfluidic Channel: The T-Sensor." Analytical Chemistry **71**: 5340-5347.

Kamholz, A. E. and P. Yager (2002). "Molecular diffusive scaling laws in pressure-driven microfluidic channels: deviation from one-dimensional Einstein approximations." Sensors and Actuators B: Chemical **82**(1): 117-121.

Kauffmann, E., N. C. Darnton, et al. (2001). "Lifetimes of intermediates in the beta-

sheet to alpha -helix transition of beta-lactoglobulin by using a diffusional IR mixer." Proceedings of the National Academy of Science **98**(12): 6646-6649.

Kennedy, M. J., S. J. Stelick, et al. (2009). "Hydrodynamic focusing with a microlithographic manifold: controlling the vertical position of a focused sample." Microfluidics and Nanofluidics **7**(4): 569-578.

Kummrow, A., J. Theisen, et al. (2009). "Microfluidic structures for flow cytometric analysis of hydrodynamically focussed blood cells fabricated by ultraprecision micromachining." Lab on a Chip **9**(7): 972-981.

Lauchlicht, B., P. Cheifetz, et al. (2008). "Evaluation of continuous flow nanosphere formation by controlled microfluidic transport." Langmuir **24**(17): 9717-9726.

Lima, R., S. Wada, et al. (2006). "Confocal micro-PIV measurements of three-dimensional profiles of cell suspension flow in a square microchannel." Measurement Science and Technology **16**: 797-808.

Lipman, E. A., B. Schuler, et al. (2003). "Single-Molecule Measurementsof Protein Folding Kinetics." Science **301**(5637): 1233-1235.

Mao, X., S. C. Lin, et al. (2009). "Single-layer planar on-chip flow cytometer using microluidic drifting based three-dimensional (3D) hydrodynamic focusing." Lab on a Chip **9**(11): 1583-1589.

Press, W. H., B. P. Flannery, et al. (1986). Numerical Recipes. New York, Cambridge University Press.

Radomsky, M. L., K. J. Whaley, et al. (1990). "Macromolecules released from polymers: diffusion into unstirred fluids." Biomaterials **11**: 619-624.

Shin, S.-J., J.-Y. Park, et al. (2007). ""On the fly" continuous generation of alginate fibers using a microfluidic device." Langmuir **23**(17): 9104-9108.

Swaminathan, R., C. P. Hoang, et al. (1997). "Photobleaching Recovery and Anisotropy Decay of Green Fluorescent Protein GFP-S65T in Solution and Cells:

Cytoplasmic Viscosity Probed by Green Fluorescent Protein Translational and Rotational Diffusion." Biophysical Journal **72**: 1900-1997.

Vamos, C., N. Suciu, et al. (2003). "Generalized random walk algorithm for the numerical modeling of complex diffusion processes." Journal of Computational Physics **186**(2): 527-544.

Zhang, S. and J. Jin (1996). Computation of Special Functions. New York, John Wiley & Sons, Inc.